Copyright Warning & Restrictions

The copyright law of the United States (Title 17, United States Code) governs the making of photocopies or other reproductions of copyrighted material.

Under certain conditions specified in the law, libraries and archives are authorized to furnish a photocopy or other reproduction. One of these specified conditions is that the photocopy or reproduction is not to be "used for any purpose other than private study, scholarship, or research." If a, user makes a request for, or later uses, a photocopy or reproduction for purposes in excess of "fair use" that user may be liable for copyright infringement,

This institution reserves the right to refuse to accept a copying order if, in its judgment, fulfillment of the order would involve violation of copyright law.

Please Note: The author retains the copyright while the New Jersey Institute of Technology reserves the right to distribute this thesis or dissertation

Printing note: If you do not wish to print this page, then select "Pages from: first page # to: last page #" on the print dialog screen

NJIT
New Jersey's Science &
Technology University

The Van Houten library has removed some of the personal information and all signatures from the approval page and biographical sketches of theses and dissertations in order to protect the identity of NJIT graduates and faculty.

ABSTRACT

DEVELOPMENT AND CHARACTERISTICS OF CARBON NITRIDE THIN SOLID FILMS FOR ADVANCED COATING APPLICATIONS

by
Muhammad A. Hussain

Carbon nitride films were synthesized on silicon substrate by reactive magnetron sputtering of graphite target in an environment of Ar and nitrogen gas. The performance of a negative carbon ion source was also investigated to use the source in negative ion-beam-assisted deposition. These films were synthesized at room temperature at a constant pressure of 5 mtorr and at 300 Watts RF power, but at different composition of nitrogen in Ar-N_2 gas mixture ranging from 0-53 percent. The films deposited were microscopically smooth, amorphous and their properties found to be varied with nitrogen composition in plasma. The deposition rate was observed to increase with RF power and decrease with chamber pressure. Flux of charged species toward the substrate was also seen to increase with RF power but relatively less sensitive to chamber pressure. The scratch resistance of the film was found to be 0.35 N at 23 percent nitrogen in plasma and increased with higher nitrogen composition. The microhardness of the film was measure to be about 14 GPa at 23 percent nitrogen composition in plasma was observed to decrease with higher nitrogen composition.

DEVELOPMENT AND CHARACTERISTICS OF CARBON NITRIDE THIN SOLID FILMS FOR ADVANCED COATING APPLICATIONS

By
Muhammad A. Hussain

A Thesis
Submitted to the Faculty of
New Jersey Institute of Technology
in Partial Fulfillment of the Requirements for the Degree of
Master of Science in Chemical Engineering

Department of Chemical Engineering, Chemistry, and Environmental Science

January 1998

Blank Page

APPROVAL PAGE

DEVELOPMENT AND CHARACTERISTICS OF CARBON NITRIDE THIN SOLID FILMS FOR ADVANCED COATING APPLICATIONS

Muhammad A. Hussain

Dr. Roland A. Levy, Thesis Advisor | Date
Distinguished Professor of Physics, NJIT

Dr. Gary S. Tompa, Committee member | Date
President, SMI, Inc.

Dr. Sergey A. Korenev, Committee member | Date
Research Professor of Physics, NJIT

BIOGRAPHICAL SKETCH

Author: Muhammad A. Hussain

Degree: Master of Science

Date: January 1998

Undergraduate and Graduate Education:

- Master of Science in Chemical Engineering,
  New Jersey Institute of Technology,
  Newark, New Jersey, 1998.

- Bachelor of Science in Chemical Engineering,
  Bangladesh University of Engineering and Technology,
  Dhaka, Bangladesh, 1993.

Major: Chemical Engineering

To my beloved family

ACKNOWLEDGEMENT

The author would like to express his sincere gratitude to his advisors, Professor Roland A. Levy, Dr. Gary S. Tompa, and Dr. Sergey A. Korenev for their guidance, suggestions, encouragement, and financial support throughout this research.

The author appreciates the timely help and suggestions from the co-workers at Structured Materials Industries, Inc., including Dr. Ivan H. Murzin, Dr. Ganesh Skandan, Dr. Yabo Li, and Bill Good. Special thanks to the CVD laboratory members at NJIT, including Dr. Vladimir Zaitsev, Vitaly Saigol, Narahari Ramanuja, Krit Aryusook, Chenna Rabindranath for their coopeartion.

The author sincerely acknowledges the support, and patience of his wife Shamima Hussain and son Shabab Hussain during this work.

Finally, the author would like to acknowledge Dr. Robert Reeber of Army Research Office, who managed the work under the contract BMDO DAAH04-95-C-0042.

TABLE OF CONTENTS

Chapter | Page

1. INTRODUCTION 1

1.1 Introduction to Superhard Materials 1

1.1.1 Introduction to Hardness 2

1.2 Prediction of New, Hard Material Based on Bulk Moduli 4

1.2.1 Prediction of β-C_3N_4 and Its Properties 6

1.3 The Objectives of this Thesis 8

2. TECHNIQUES FOR THIN FILM DEPOSITION 10

2.1 Introduction 10

2.2 Chemical Vapor Deposition 10

2.3 Physical Vapor Deposition 12

2.3.1 Evaporation 12

2.3.2 Sputtering 13

2.3.2.1 Fundamentals of Glow Discharges 13

2.3.2.1.1 DC Glow Discharges 13

2.3.2.1.2 Discharge Species 15

2.3.2.1.3 Collision Processes 18

2.3.2.2 Sputtering Processes 21

2.3.2.2.1 Introduction 21

2.3.2.2.2 Sputter Yield 23

2.3.2.2.3 Thermal History of the Substrate 25

TABLE OF CONTENTS
(Continued)

Chapter **Page**

2.3.2.3 Types of Sputtering Processes 26

2.3.2.3.1 DC Sputtering 26

2.3.2.3.2 RF Sputtering 27

2.3.2.3.3 Magnetron Sputtering 29

2.3.2.3.3.1 Electron Motion in Perpendicular Electric and Magnetic Field 30

2.3.2.3.4 Reactive Sputtering 31

2.3.2.4 Evaporation vs. Sputtering 34

2.3.3 Hybrid and Modified PVD Processes 35

2.3.3.1 Ion-Beam-Assisted Deposition Processes 35

2.4 Film Formation Mechanism 36

3. RIVIEW OF LITERATURE 38

3.1 Technical Barrier to Synthesize Carbon Nitride Thin Films 38

3.2 Results to Date to Synthesize β-C_3N_4 39

4. EXPERIMENTS 45

4.1 Introduction 45

4.2 Sputtering System 45

4.3 Negative Carbon Ion Source 48

4.4 Deposition Procedure 49

4.4.1 Leakage Check 49

TABLE OF CONTENTS
(Continued)

Chapter **Page**

4.4.2 Loading Substrates 49

4.4.3 Deposition 50

4.5 Characterization of Carbon Nitride Thin Films 51

4.5.1 Scratch Resistance 51

4.5.2 Hardness and Young's Modulus 51

4.5.3 Raman Scattering 53

5. RESULTS AND DISCUSSIONS 54

5.1 Introduction 54

5.2 Plasma Characteristics 54

5.3 Characterization of Film 59

5.4 Characterization of Cs Enhanced Negative Carbon Ion Source 63

6. CONCLUSIONS 69

REFERENCES 70

LIST OF TABLES

Table	Page
1.1 Values of Bulk Modulus of Different Types of Solids	4
1.2 Calculated Bulk Moduli and Microhardness for Light, Superhard, and Covalent Ceramics	7
2.1 Evaporation vs. Sputtering	34
3.1 The Summary of Results on Synthesis of Carbon Nitride Obtained Worldwide	43

LIST OF FIGURES

Figure **Page**

1.1 Structure of β-C_3N_4 in the a-b plane. The c axis is normal to the page. Half the atoms illustrated are located in the z = c/4 plane. The parallelogram shows the unit cell 6

2.1 Luminous region of the dc glow discharge 14

2.2 Voltage distribution across dc glow discharge 17

2.3 Schematic of simplified sputtering system: (a) dc, (b) RF 22

2.4 Ion-solid interaction during sputtering 22

2.5 Applied fields and electron motion in the planar magnetron 30

2.6 Generic hysteresis curve for system pressure vs. Reactive gas flow Rate during reactive sputtering 32

2.7 Formation of a thin film 37

4.1 Schematic of carbon nitride thin film deposition system 46

4.2 Cross-sectional schematic of a negative carbon ion source 48

5.1 Variation of deposition rate with chamber pressure (with pure Ar plasma) 55

5.2 Variation of current absorbed at the susbstrate with chamber pressure At different RF power (with pure Ar plasma) 56

5.3 Variation of deposition rate and current absorbed at the susbstrate With nitrogen composition in Ar-N_2 gas mixture (at 150 W and 5 mTorr pressure 57

5.4 Hysteresis plot for reactive sputtering of carbon with Ar-N_2 plasma 58

5.5 Variation of critical force with nitrogen composition in Ar-N_2 plasma 59

5.6 Variation of microhardness of the film with N_2 composition in Ar-N_2 plasma 60

LIST OF FIGURES
(Continued)

Figure **Page**

5.7 Dependence of Young's modulus on nitrogen composition in $Ar-N_2$ Plasma ... 62

5.8 Raman spectra of carbon nitride thin film (deposited at 300 Watts RF power, 5 mtorr pressure, 23% nitrogen in $Ar-N_2$ plasma and at 4 sccm of N_2 flow rate) ... 63

5.9 Dependency of absorbed current at the substrate on cesium oven temperature ... 64

5.10 Variation of deposition rate with cesium oven temperature ... 65

5.11 Current absorbed at substrate vs. Chamber pressure ... 66

5.12 Variation of current absorbed at the substrate with positive bias Voltage applied at ion extraction lens ... 67

CHAPTER 1

INTRODUCTION

1.1 Introduction to Superhard Materials

Materials with microhardness exceeding 4000 kg-mm^{-2} on the Knoop scale may be defined as "superhard materials" [1]. There are only two confirmed phases of superhard materials: diamond (α-C), with a microhardness of about 9000 kg-mm^{-2}, and cubic boron nitride (β-BN or c-BN), of about 4800 kg-mm^{-2}.

Superhard materials posses a unique combination of superior properties such as highest: compressional strengths, thermal conductivities, spectral transmittances, hole mobilities, and sound speeds. The refractive indices and chemical inertness of these materials are also among the highest. The mix of all these properties accompanied with extremely low coefficients of thermal expansion and mechanical friction makes superhard materials highly desirable as industrial materials. The uses of superhard materials include heat sinks, gem stones, radiation windows, speaker tweeters, mechanical bearings, surgical knives, container coatings, and potentially semiconductors. The leading industrial application of superhard materials so far is superabrasives, which has a worldwide annual consumption of approximately two tons with a total value of about one billion US dollars. Nonabrasive applications of superhard materials are predicted to outweigh those of superabrasives by the end of this century.

1.1.1 Introduction to Hardness

Hardness is an important material property of concern in films utilized for electronic and optical as well as mechanically functional applications. It is a complex property related to the extent to which solids resist both elastic and plastic deformations [1]. For materials with defects, hardness can be limited by many factors including point defects, dislocations and macroscopic defects. On the microscopic system, for ideal systems, hardness is determined by the bulk modulus, which in turn depends on the nature of chemical bonding. It is the strength and compressibility of the bond that plays the primary role in a solid's ability to resist deformation.

The upper limit of hardness is determined by the rigidity of a material's crystal structure. There are three factors that contribute to the rigidity of a crystal structure: (1) large coordination number (CN) of the atoms, (2) high covalent character of bonds, and (3) short interatomic distance of the structure, i.e., small atoms. The combined effect of these three factors is to concentrate the bond energy in a small volume, so a large stress is required to deform the crystal lattice.

Covalent bonds are the strongest among all types of bonds (covalent, ionic, metallic, and Van der Waals). Covalent bonds are directional and are so strong that they can prevent atoms from sliding against one another. Coordination number is limited to 4 for covalent bonds in naturally occurring materials, although it can be as large as 12 for metallic bonds and 8 for ionic bonds. Four bonds are also the least needed to support an atom in three dimensions. This is because four bonds can define a tetrahedron, the simplest polyhedron. The tetrahedral structures are the basis of superhard materials.

Choosing a scale of hardness can also be complex and depends on the method used for measurement. Mohs' empirical scale, which ranges from talc (1) to calcite (3) to quartz (7) up to diamond (10), implies that the hardness of diamond, like the speed of light, will not be exceeded. Hardness is often measured by indentation methods. Hardness so measured is called microhardness of which Vickers and Knoop are common scales. The Vickers hardness test, also known as the diamond pyramid hardness test (DPH) test, employs an indenter consisting of a square-based diamond pyramid ground to have a face angle of 136^0. The Vickers hardness number H_v is obtained as the ratio of applied load L to the surface area of the resulting indentation. It is given by

$$H_v = \frac{1.854L}{l_v^2} \text{ Kg/mm}^2 \quad (1.1)$$

where l_v is the indentation diagonal. A related test is the Knoop microhardness test, which employs a rhombic-based diamond pyramid indenter where the length ratio of the major to minor indentation diagonal is 7:11, furthermore, the minor diagonal is four times the penetration depth. The Knoop hardness is given by

$$H_k = \frac{14.22L}{l_k^2} \text{ Kg/mm}^2 \quad (1.2)$$

where l_k is the length of the major indentation diagonal. Care must be taken in distinguishing H_v and H_k values, which are sometimes used interchangeably, even though the former are some 10-15% lower than the latter.

1.2 Prediction of New, Hard Material Based on Bulk Modulus

Isothermal bulk modulus (coefficient of incompressibility) of a material measures its resistance to volume reduction under compression [1]. Mathematically,

$$B = -V\left(\frac{\partial P}{\partial V}\right) \qquad (1.3)$$

where V and P represent volume and pressure. The upper limit of bulk modulus of a material reflects the intrinsic compressive hardness of a crystal structure. The bulk modulus is measured in the pressure unit gigapascal (1GPa = 10,000 bar). Approximate values of B for different types of solids are given in Table 1.1

Table 1.1 Values of Bulk Modulus of Different Types of Solids

Type of solid	Approximate values of B (GPa)
Rare gas solids	1 to 2
Ionic solids	10 to 60
Simple metals	2 to 100
Transition metals	100 to 300
Covalent solids	100 to 443

Bulk modulus is very difficult to measure and therefore it is not used as a common scale of hardness. However, a semi-empirical approach [2] was developed and first applied to group IV, III-V, II-VI tetrahedrally bonded materials composed of atoms

from the center of the periodic table. For bond lengths d, expressed in angstroms, B is given [2] in gigapascals by

$$B = \frac{N_c(1972 - 220I)}{4d^{3.5}} \tag{1.4}$$

where N_c is the coordination number. An empirical ionicity parameter $I = 0$, 1, and 2 for groups IV, III-V, and II-VI solids, respectively, accounts for the reduction in B arising from increased charge transfer. N_c is the average coordination number for the system under investigation and for tetrahedral system $N_c = 4$.

The semi-empirical law given by equation (1.4) successfully describes the diamond and zinc blende semiconductors, giving results for the bulk moduli within a few percent of theoretical value. This approach also suggests that large values of B can be obtained by minimizing ionicity and bond length. With $I = 1$ and $d = 1.56$ A, the semi-empirical scaling law yields $B = 3.67$ Mbar for BN. A measurement [3] of the bulk modulus of BN yields 3.69 Mbar. The good quantitative agreement of the results of the empirical model and experiment demonstrate the predictive power of the model. Theoretical calculation of B can also be performed by (1) calculating the total energy of the solid structure as a function of cell volume, and (2) fitting the energy vs. cell volume data in an equation of state.

1.2.1 Prediction of β-C_3N_4 and Its Properties

Based on the semi-empirical model, it was suggested that a covalent solid formed between C and N could have a larger bulk modulus than diamond [2]. As a prototype, a complex structure of a C-N solid was chosen on the basis of the known β-Si_3N_4 structure with C substituted for Si. The octet rule for covalent bonding is satisfied in this structure. In Fig. 1, the structure is shown to consist of buckled layers stacked in an AAA... sequence [4]. The hexagonal unit cell contains two formula units (14 atoms) with local

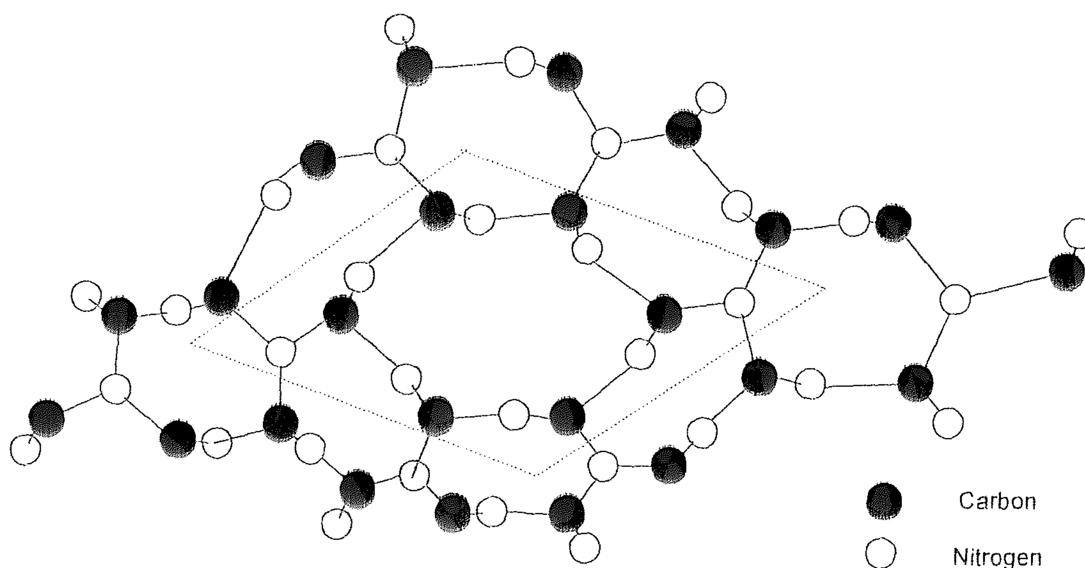

Figure 1.1 Structure of β-C3N4 in the a-b plane. The c axis is normal to the page. Half the atoms illustrated are located in the z = -c/4 plane, the other half are in the z= c/4 plane. The parallelogram shows the unit cell

order such that C atoms occupy slightly distorted tetrahedral sites while N atoms sit in nearly planar triply coordinated sites. This kind of atomic arrangement suggests that C

atoms are sp^3 hybridized whereas N atoms are sp^2 hybridized. Although the lack of complete tetrahedral coordination suggests that semi-empirical scaling law may not be as precise as in the diamond and zinc blende cases, it was expected that the trends contained in the scaling law would be followed. A listing of properties of β-C_3N_4 and of other superhard materials are listed in Table 1.2.

Table 1.2 Calculated Bulk Moduli and Microhardness for Light, Superhard and Covalent Ceramics

Material	Bond Length (Angstrom)	Coordination Number	Bulk Modulus (GPa)	Knoop Hardness (kg-mm^{-2})
C(diamond)	1.54	4	443.0	7690
C_3N_4	1.47	3.43	427.0 ± 15*	7300
BC_2N	1.555	3.5	406.5	700
BCN	1.567	3.33	388.2	6660
BN	1.57	3	367.0	6250
C_3Si	1.71	4	295.1	4700
B_4C_3	1.666	3.43	272.3	4470
BC_2P	1.755	3.5	257.6	4190

*Theoretical value, theory in general underestimates this value. So it could indeed be harder than diamond.

The structural properties of hypothetical β-C_3N_4 are determined by calculating the total crystal energy as a function of volume. At the equilibrium volume, the cohesive energy is reported to be 81 eV per cell or on an average value of 5.8 eV per atom [4]. This moderately large cohesive energy (β-Si_3N_4 has a cohesive energy of 74.3 eV per cell) suggests that there is a good chance that β-C_3N_4 is at least a metastable structure. Again for the calculated bond length and an estimated ionicity factor of I=1/2, the semi-empirical scaling law overestimates the bulk modulus of β-C_3N_4 by about 10%. Similar overestimate is found for the bulk modulus of β-Si_3N_4. These overestimates are reported to be caused by the structural difference between these materials and the zinc blende structure on which scaling law is based on. The theoretical calculations have revealed not only other phases such as α-, cubic, pseudocubic-, graphitic- C_3N_4 with the highest bulk modulus of 496 GPa in cubic- C_3N_4 (435 GPa calculated and 443 measured for diamond) [6], but also wide band gap, about 6.3 eV [5], which is larger than that of diamond (5.5 eV). This wide band gap means that β-C_3N_4 can be an excellent electrical insulator and superior thermal conductor.

1.3 The Objectives of this Thesis

The theoretical prediction of superhardness of β- C_3N_4 have motivated intense theoretical calculations [2-6] and a great deal of experimental efforts to synthesize films of the hypothetical diamond-hard β-C_3N_4 compound. The techniques studied are plasma decomposition [7], pyrolysis [8, 9], shock wave compression [10], high pressure/high

temperature compaction [11], IBAD and sputtering [12, 13], laser ablation [14, 15] and very recently hot filament CVD [16-19]. This is a great challenge both for the application of first-principle calculations in the material science and the development of synthesis techniques.

In this study, carbon nitride thin films were synthesized by radio frequency (13.56 MHz) reactive magnetron sputtering. Ar gas was used as a working gas to ignite and sustain a plasma inside the chamber. Nitrogen gas was used as a reactive gas. Deposition rate and current absorbed at the substrate were characterized for different process parameters such as pressure, RF power and nitrogen composition in Ar-N_2 gas mixture etc. Carbon nitride thin films were synthesized mostly at 300 watts. The effect of nitrogen composition in Ar-N_2 gas mixture on mechanical properties of the film was investigated.

The performance of a cesium enhanced negative carbon ion source designed and manufactured at SMI, Inc. was also investigated to study negative ion beam assisted deposition of carbon nitride thin films. Since cesium has the lowest ionization potential (3.893 V) and it reduces the surface work function of the carbon source target, hence deposition of a monolayer of cesium on the carbon target enhances formation of negatively charged carbon ions.

CHAPTER 2

TECHNIQUES FOR THIN FILM DEPOSITION

2.1 Introduction

Depending on the mechanism of formation of deposition product on the substrate, basic thin film deposition processes can be divided into two major categories: (1) Chemical vapor deposition (CVD) and (2) Physical vapor deposition (PVD). Physical vapor deposition includes both evaporation and sputtering. Some factors that distinguish PVD from CVD are [20]:

1) Reliance of PVD processes on solid or molten sources
2) Physical mechanisms (evaporation or collisional impact) by which source atoms enter the gas phase in PVD processes
3) Reduced pressure environment through which the gaseous species are transported in PVD processes
4) General absence of chemical reactions in the gas phase and at the substrate surface (reactive PVD processes are exception)

2.2 Chemical Vapor Deposition

Chemical vapor deposition (CVD) is the process of chemically reacting a volatile compound of a material to be deposited, with other gases, to produce a nonvolatile solid that deposits atomistically on a suitably placed substrate [20]. High-temperature CVD processes for producing thin films and coatings have found increasing applications in

such diverse technologies as the fabrication of solid-state electronic devices, the manufacture of ball bearings and cutting tools, and the production of rocket engine and nuclear reactor components. In particular, the need for high-quality epitaxial semiconductor films for both Si bipolar and MOS transistors, coupled with necessity to deposit various insulating and passivating films at low temperatures, has served as a powerful impetus to spur development and implementation of CVD processes.

Among the reasons for the growing adoption of CVD methods is the ability to produce a large variety of films and coating of metals, semiconductors and compounds in either a crystalline or vitreous form, possessing high purity and desirable properties. Other advantages include relatively low cost of equipment and operating expenses, suitability for both batch and semi-continuous operation, and compatibility with other processing steps. The variants of CVD processes include atmospheric pressure (APCVD), low pressure (LPCVD), plasma-enhanced (PECVD), metal organic (MOCVD), and laser-enhanced (LECVD) chemical vapor deposition.

Various types chemical reaction which have been employed to deposit films and coatings are [20]: (1) Pyrolysis, (2) Reduction, (3) Oxidation, (4) Compound formation, (5) Disproportionation, and (6) Reversible transfer.

2.3 Physical Vapor Deposition

Physical vapor deposition includes two of the most important methods for depositing thin films, evaporation and sputtering. The objective of these deposition processes is to controllably transfer atoms from a source to a substrate where film formation and growth proceed atomistically.

2.3.1 Evaporation

In evaporation, atoms are removed from the source by thermal means, whereas in sputtering they are dislodged from solid target (source) surfaces through impact of gaseous ions.

Advances in the development of vacuum-pumping equipment and the fabrication of suitable Joule heating sources spurred the progress of evaporation technology. Higher deposition rates, better vacuum, and thus, cleaner environments for film formation and growth, and general applicability to all classes of materials were some of the reason for the ascendancy of evaporation methods. However, films used for magnetic and microelectronic applications necessitated the use of alloys and compounds, with stringent stoichiometry limits, which had to conformally cover and adhere well to substrate surfaces.

2.3.2 Sputtering

Before introducing sputtering, an important and complex thin film deposition technique, the author would like to present a brief discussion on the fundamentals of glow discharge or plasma for a better understanding of the process.

2.3.2.1 Fundamentals of Glow Discharges

2.3.2.1.1 DC Glow Discharges: The manner in which a glow discharge progresses in a low-pressure gas using a high-impedence dc power supply is quite complex. Initially a very small current flows due to the small number of initial charge carriers in the system. As the voltage is increased, sufficient energy is imparted to the charged particles to create more carriers. This occurs through ion collisions with the cathode, which release secondary electrons, and by impact ionization of neutral gas atoms. With charge multiplication, the current increases rapidly but the voltage, limited by the output impedence of the power supply, remains constant. This regime is known as the Townsend discharge. Large number of electrons and ions are created through avalanches. Eventually, when enough of the electrons generated produce sufficient ions to regenerate the same number of initial electrons, the discharge becomes self-sustaining. The gas begins to glow now, and the voltage drops, accompanied by a sharp rise in current. At this state "normal glow" occurs. Initially, ion bombardment of the cathode is not uniform but is concentrated near the cathode edges or at other surface irregularities. As more power is applied, the bombardment increasingly spreads over the entire surface until a nearly uniform current density is achieved. A further increase in power results in higher voltage and current density levels. The "abnormal discharge" regime has now been

entered and this is the operative domain for sputtering and other discharge processes. At still higher currents, low voltage arcs propagate.

Adjacent to the cathode is the highly luminous cathode glow layer . The light emitted depends on the incident ions and the cathode material. In this region, neutralization of the incoming discharge ions and positive cathode ions occurs. Secondary electrons start to accelerate away from the cathode. In between is the Crookes dark space where nearly all of the applied voltage is dropped. Within the dark space, the positive gas ions are accelerated toward the cathode. The next distinctive region is the "negative glow", where the accelerated electrons acquire enough energy to impact-ionize the neutral gas molecules. Beyond this is the Faraday's dark space and finally the positive column [20]. The discharge regimes is schematically depicted in Fig. 2.1.

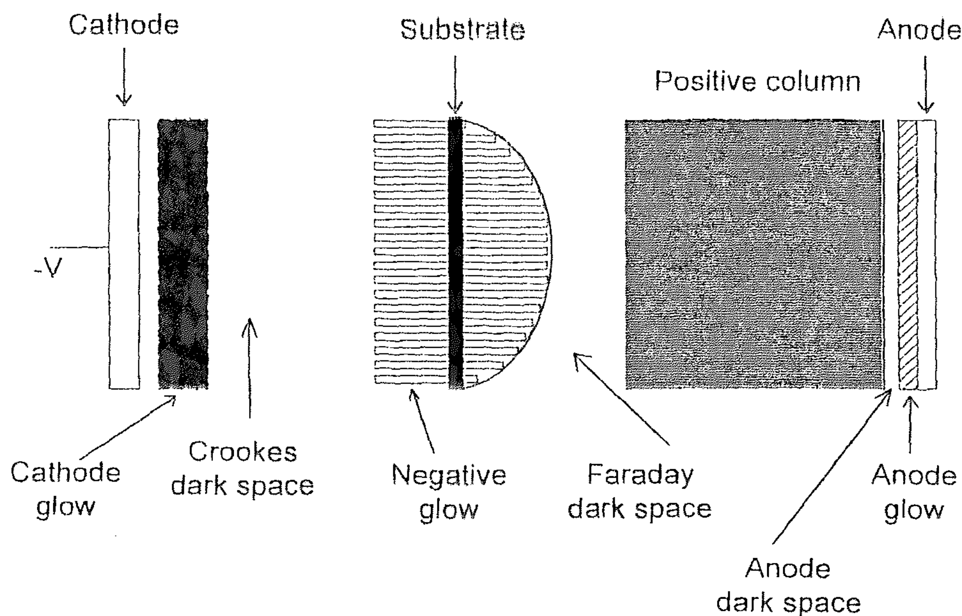

Figure 2.1: Luminous region of the dc glow discahrge

2.3.2.1.2 Discharge Species: A discharge is essentially a plasma-i.e., a partially ionized gas composed of ions, electrons, and neutral species that is electrically neutral when averaged over all the particles contained within [20]. Coulombic interaction enables the charged species to behave in a fluid-like fashion and determines many of the plasma properties. In plasmas used in sputtering, the particle density is low enough, and the fields are sufficiently strong so that neutrals are not in equilibrium with electrons. Typically, the degree of ionization or ratio between number of ions and neutrals is about 10^{-4}. Measurements on glow discharge yield average electron energies of about 2 eV. The effective temperature T associated with a given energy E is simply given by T = E/k. where k is the Boltzmann constant. Substituting, it is found that electrons have an astoundingly high temperature of some 23,000 K. However, because there are so few of them, their heat content is small and the chamber walls do not heat appreciably. Neutrals and ions are not nearly as energetic; the former have energies of only 0.025 eV (or T = 290 K) and the latter, energies of $\sim$ 0.04 eV (or T = 460 K). Ions have higher energies than neutrals because they acquire energy from the applied electric field.

Since surfaces (e.g., targets, substrates) are immersed in the plasma, they are bombarded by the species present. The neutral particle flux can be calculated from the following equation

$$\phi = \frac{3.513 \times 10^{22} P}{\sqrt{MT}} \text{ Molecules/cm}^2\text{-sec} \qquad (2.1)$$

where pressure P is expressed in torr, M is the molecular weight of gas with which plasma is generated, and T is the temperature expressed in K. Charged particle impingement results in an effective current density J_i given by the product of the particle

flux and the charge q_i transported. Therefore,

$$J_i = \frac{n_i q_i \overline{v_i}}{4} \tag{2.2}$$

where n_i, $\overline{v_i}$ are the specie concentration and mean velocity, respectively. $\overline{v_i}$ can be calculated from the following equation

$$\overline{v_i} = \left(\frac{8kT}{\pi m}\right)^{1/2} \tag{2.3}$$

For electrons, $m = 9.1 \times 10^{-28}$ g, and assuming $T = 23{,}000$ K and $n = 10^{10}/\text{cm}^3$, $J_{electron} \sim 38$ mA/cm^2. The ions, present in the same amounts as electrons, are much heavier and have a lower effective temperature than the electrons. This accounts for their very low velocity compared with that of electrons. For example, $v_{ion} = 5.2 \times 10^4$ cm/sec for Ar ions as well as neutral atoms, whereas for electrons $v_{electron} = 9.5 \times 10^7$ cm/sec. The ion current is correspondingly reduced relative to the electron current by the ratio of these velocities, so $J_{ion} = 21$ μA/cm^2. The implication of this simple calculation is that an isolated surface within the plasma charges negatively initially. Subsequently, additional electrons are repelled and positive ions are attracted. Therefore, the surface continues to charge negatively at a decreasing rate until the electron flux equals the ion flux and there is no net steady-state current.

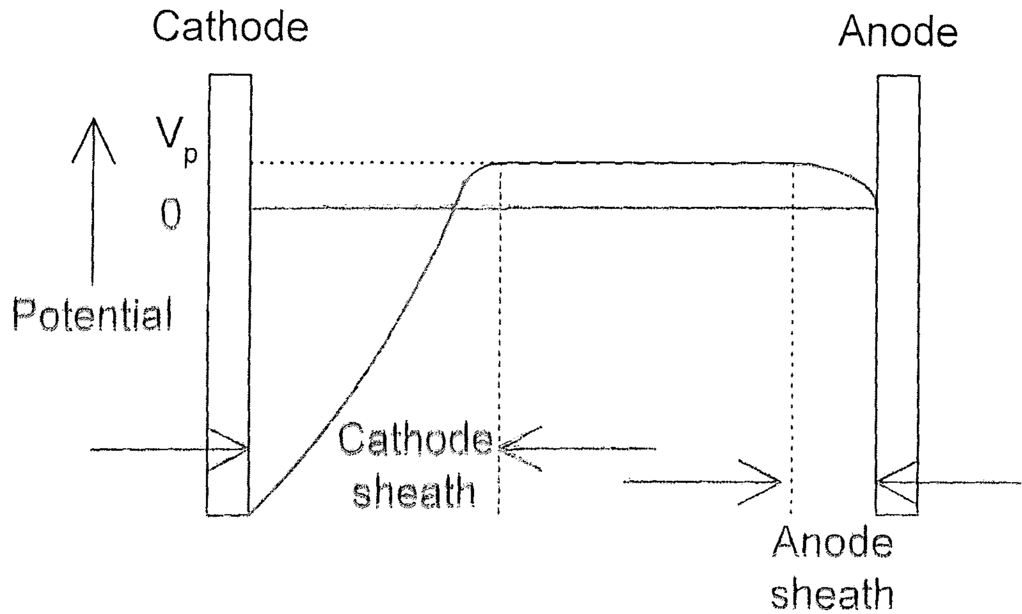

Figure 2.2: Voltage distribution across dc glow discharge

The anode and cathode, in the glow discharge, are then expected to be at a negative potential with respect to the plasma. The voltage distribution in a dc glow discharge under these conditions is shown schematically in Fig. 2.2. A sheath develops around each electrode with a net positive space charge. The lower electron density in the sheath means less ionization and excitation of neutrals. Hence, there is less luminosity there than in the glow itself. Electric fields (derivative of the potential) are restricted to the sheath regions. The plasma itself is not at a potential intermediate between that of the electrodes but is typically some 10 V positive with respect to the anode at zero potential. Sheath width dimensions depend on the electron density and temperature. Using the values given earlier for the electrically isolated surface, it can be calculated to be about 100 μm. It is the sheath-plasma interface that ions begin to accelerate on their way to the

target during sputtering; electrons, however, are repelled from both sheath regions. All of these unusual charge effects stem from the fact that the fundamental plasma particles (electrons and ions) have such different masses and, hence, velocities and energies.

2.3.2.1.3 Collision Processes: Collisions between electrons and all the other species (charged or neutral) within the plasma dominate the properties of the glow discharge. Collisions are elastic and inelastic, depending on whether the internal energy of the colliding species is preserved. The well-known result of elastic binary collision is

$$\frac{E_2}{E_1} = \frac{4 M_1 M_2 \cos^2 \theta}{(M_1 M_2)^2} \qquad (2.4)$$

where 1 and 2 refer to the two particles of mass M_1, energy E_1 and mass M_2, energy E_2 respectively. It is assumed that M_2 is initially stationary and M_1 collides with it at an angle θ defined by the initial trajectory and the line joining their centers at contact. The quantity $4 M_1 M_2 / (M_1 + M_2)^2$ is known as the energy transfer function. When $M_1 = M_2$, it has a value of 1; i.e., after collision the initial moving projectile remains stationary, and all of its energy is efficiently transferred to the second particle, which speeds away. When, however, $M_1 << M_2$, then the energy transfer function is ~ $4 M_1 / M_2$ and has a typical value of ~ 10^{-4}. Little kinetic energy is transferred in the collision of the light electron with the massive nitrogen atom.

For inelastic collision, the maximum fraction of kinetic energy transferred is given by

$$\frac{\Delta U}{(1/2)M_1 v_1^2} = \frac{M_2}{(M_1 + M_2)} \cos^2\theta \qquad (2.5)$$

where v_1 is the initial velocity of particle 1. For the inelastic collision between an electron and nitrogen molecule, $\Delta U/(1/2)M_1 v_1^2 \approx 1$, when $\cos\theta = 1$. Therefore, contrary to an elastic collision, virtually all of an electron's kinetic energy can be transferred to the heavier species in the elastic collision.

1. The rich diversity of inelastic collisions and chemical processes that occur in plasma and generally enhance film deposition and etching processes are summarized as follows:Ionization. The most important process in sustaining the discharge is electron impact ionization. A typical reaction is

$$e^- + Ar^0 \rightarrow Ar^+ + 2e^- \qquad (2.6)$$

2. Excitation. In this case the energy of the electron excites quantitized transitions between vibrational, rotational, and electronic states, leaving the molecule in an excited state (denoted by an asterisk). An example is

$$e^- + O_2^0 \rightarrow O_2^* + e^- \qquad (2.7)$$

3. Dissociation. In dissociation, the molecule is broken into smaller atomic or molecular fragments. The products (radicals) are generally much more chemically active than the parent gas molecule and serve to accelerate reactions. Dissociation of CF_4, for example, is relied on in plasma etching or film removal processes i.e.,

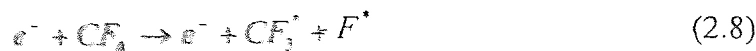

$$e^- + CF_4 \rightarrow e^- + CF_3^* + F^* \qquad (2.8)$$

4. Dissociative Ionization. During dissociation one of the excited species may become ionized; e.g.,

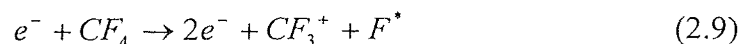

$$e^- + CF_4 \rightarrow 2e^- + CF_3^+ + F^* \qquad (2.9)$$

5. Electron Attachment. Here neutral molecules become negative ions after capturing an electron. For example,

$$e^- + SF_6^0 \rightarrow SF_6^- \qquad (2.10)$$

6. Dissociative Attachment.

$$e^- + N_2^0 \rightarrow N^+ + N^- + e^- \qquad (2.11)$$

In addition to electron collisions, ion-neutral as well as excited or metastable-excited, and excited atom-neutral collisions occur. Some generic examples of these reactions are as follows:

7. Symmetrical Charge Transfer.

$$A + A^+ \rightarrow A^+ + A \qquad (2.12)$$

8. Asymmetric Charge Transfer.

$$A + B^+ \rightarrow A^+ + B \qquad (2.13)$$

9. Metastable-Neutral.

$$A^* + B \rightarrow B^+ A + e^- \qquad (2.14)$$

10. Metastable-Metastable Ionization.

$$A^* + A^* \rightarrow A + A^+ + e^- \qquad (2.15)$$

2.3.2.2Sputtering Processes

2.3.2.2.1 Introduction: Sputtering is a complex technique of thin film deposition in which energetic particles (ions, electrons etc.) establish a train of collision events in the target (a plate of materials to be deposited or the material from which a film is synthesized) leading to the ejection of a matrix atom by transfer of momentum. The target is connected to the negative terminal of a dc or RF power supply (Fig. 2.3). So it is also known as cathode. Typically several kilovolts are applied to it. The substrate that faces the cathode may be grounded, electrically floating, biased positively or negatively, heated, cooled, or some combination of these. A discharge or plasma is initiated and sustained by introducing a gas , typically argon, into the evacuated chamber. Gas pressure usually range from a few to 100 mtorr. Microscopically, positive ions in the discharge strike the cathode plate and eject neutral target atoms through momentum transfer. These atoms enter and pass through the discharge region to eventually deposit on the growing film. The effects of energetic particle bombardment on surfaces and growing film during sputtering are depicted in Fig. 2.4.

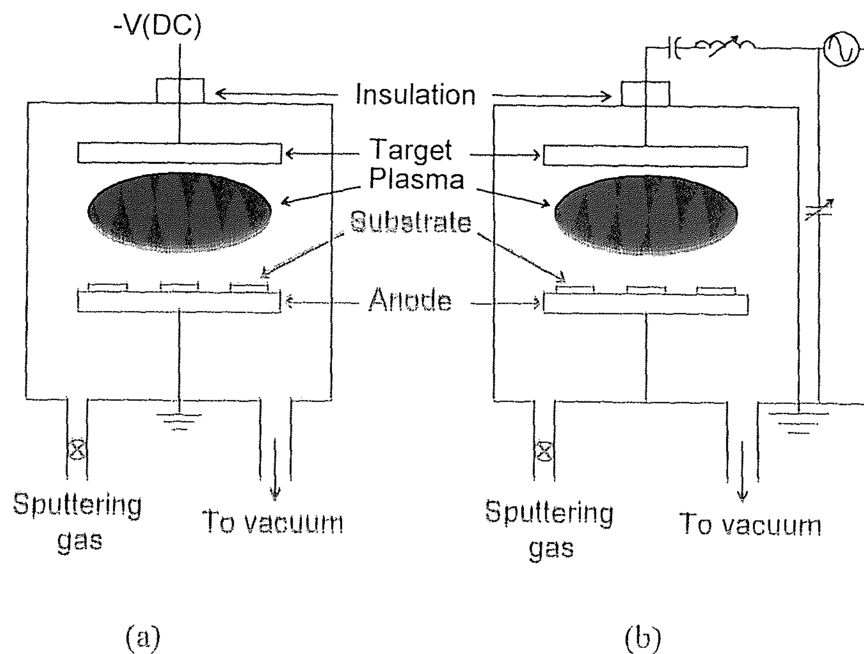

Figure 2.3: Schematic of simplified sputtering systems: (a) dc, (b) RF

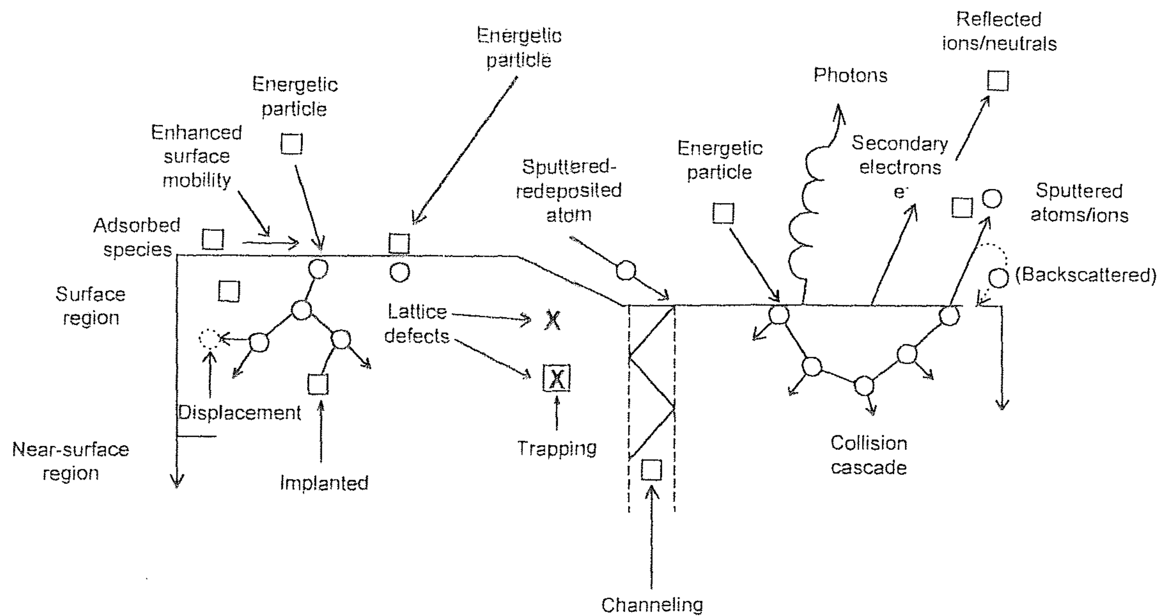

Figure 2.4: Ion-solid interactions during sputtering

Sputter yield, the most fundamental parameter characterizing sputtering, and thermal history of substrate during sputtering will be discussed next.

2.3.2.2.2 Sputter Yield: The sputter yield is denoted by S and defined as the number of atoms or molecules ejected from a target surface per incident ion and is a measure of the efficiency of sputtering. S is proportional to a product of the following factors [20]:

1. The number of atoms displaced toward the surface per primary collision. This term is given by $\overline{E}/2E_t$, where $\overline{E}$ is the mean energy of the struck target atom and E_t is the threshold energy required to displace an atom. The factor of 2 is necessary because only half of the displaced atoms move toward the surface. The quantity $\overline{E}$ may be taken as an average of E_2, the kinetic energy transferred to the target atom, and E_t; i.e.,

$$\overline{E} = \frac{E_2 + E_t}{2}, \qquad \text{where } E_2 = \frac{4M_1M_2}{(M_1 + M_2)^2}E_1$$

2. The number of atomic layers that contain these atoms and contribute to sputtering. Statistics show that the number of collisions required to slow an atom of energy $\overline{E}$ to E_b, the surface binding energy, is

$$N = \frac{\ln \overline{E}/E_b}{\ln 2} \qquad (2.16)$$

By a random walk model, the average number of contributing atomic layers is $1 + N^{1/2}$

3. The number of target atoms per unit area n_A.

4. The cross section $\sigma_o = \pi a^2$, where a is related to the Bohr radius of the atom a_b, and the atomic numbers Z_1, Z_2 of the incident ion and sputtered atom respectively; i.e.,

$$a = \frac{a_b}{\sqrt{Z_1^{2/3} + Z_2^{2/3}}}.$$

Combining terms gives

$$S = \frac{\overline{E}}{E_t}\left\{1 + \left(\frac{\ln \overline{E}/E_b}{\ln 2}\right)^{1/2}\right\}\sigma_o n_A \qquad (2.17)$$

The currently accepted theory for the sputtering yield from collision cascades is due to Sigmund [20] and predicts that

$$S = \frac{3\alpha}{4\pi^2}\frac{4M_1M_2}{(M_1+M_2)^2}\frac{E_1}{E_b} \quad (E_1 < 1\text{ keV}) \qquad (2.18)$$

and

$$S = 3.56\alpha\frac{Z_1Z_2}{Z_1^{2/3}+Z_2^{2/3}}\left(\frac{M_1}{M_1+M_2}\right)\frac{S_n(E)}{E_b} \quad (E_1 > 1\text{ keV}) \qquad (2.19)$$

These equations depend on two complex quantities, α and $S_n(E)$. The parameter α, a measure of the efficiency of momentum transfer in collisions, increases monotonically from 0.17 to 1.4 as M_1 / M_2 ranges from 0.1 to 10. The reduced stopping power, $S_n(E)$, is a measure of the energy loss per unit length due to nuclear collisions. It is a function of the energy as well as masses and atomic numbers of the atoms involved. At high energy, S is relatively constant because $S_n(E)$ tends to be independent of energy.

2.3.2.2.3 Thermal History of the Substrate: One of the important issues related to sputtering is the temperature rise in the substrate during film deposition. Sputtered atoms that impinge on the substrate are far more energetic than similar atoms emanating from an evaporation source. During condensation, this energy must be dissipated by the substrate, or else it may heat excessively, to the detriment of the quality of the deposited film. Equation 2.20, representing an unsteady-state heat power balance equation, is useful to address the question of substrate heating.

$$\rho c d(dT/dt) = P - L \tag{2.20}$$

The term on the left is the net thermal energy per unit area per unit time (in typical units of watts/cm^2) retained by a substrate whose density, heat capacity, effective thickness, and rate of temperature rise are given by $\rho, c, d,$ and dT/dt, respectively.

The incident power flux P has three important components:

1. Heat of condensation of atoms, ΔH_c (eV/atom)
2. Average kinetic energy of incident adatoms, $\overline{E_k}$ (eV/atom).
3. Plasma heating from bombardment of neutrals and electrons. The plasma energy is assumed to be E_p (eV/atom).

For a deposition rate $\dot{d}$ (Angstrom/min),

$$P = \frac{2.67 \times 10^{-29}\, \dot{d}(\Delta H_c + \overline{E}_k + E_p)}{\Omega} \text{ watts/cm}^2 \tag{2.21}$$

where Ω is the condensate atomic volume in cm^3/atom. The L term represents the heat loss to the substrate holder by conduction or to cooler surfaces in the chamber by

radiation. Neglecting L for an instance, temperature rise of a thermally isolated substrate can be calculated by substituting Eq. (2.21) into Eq (2.20) and integrating,

$$T(t) = \frac{2.67 \times 10^{-29}\, d(\Delta H_c + \bar{E}_k + E_p)t}{\rho c d\Omega} \qquad (2.22)$$

But in reality, temperature rise would be less than that calculated by equation 2.22 because of the heat loss by radiation term (L).

2.3.2.3 Types of Sputtering Processes

Sputtering processes can be divided into four categories: (1) dc, (2) RF, (3) magnetron, (4) reactive. There are, however, important variants within each category (e.g., dc bias) and even hybrid between categories (e.g., reactive RF). A brief description of each category will be presented in this section.

2.3.2.3.1 DC Sputtering: The system configuration of a conventional dc sputtering system (Fig. 2.3 (a)), the discharge environment (section 2.3.2.1.1), ion-solid interaction (Fig. 2.4), or intrinsic sputter yield (section 2.3.2.2.2) are already discussed. However, it is important to note that the relative film deposition rate depends on the sputtering pressure and current variables. At low pressures, the cathode sheath is wide and ions are produced far from the target; their chances of being lost to the walls are great. The mean-free electron path between collisions is large, and electrons collected by the anode are not replenished by ion-impact-induced cathode secondary emission. Therefore, ionization efficiencies are low, and self-sustained discharges cannot be maintained below about 10

mtorr. As the pressure is increased at a fixed voltage, the electron mean-free path is decreased, more ions are generated, and larger currents flow. But if the pressure is too high, the sputtered atoms undergo increased collisional scattering and are not efficiently deposited. In general, the deposition rate is proportional to the power consumed, or to the square of the current density, and inversely dependent on the electrode spacing.

2.3.2.3.2 RF Sputtering: A conventional RF sputtering system is already depicted schematically in Fig. 2.3 (b). RF sputtering was invented as a means of depositing insulating thin films. For example, a thin film of SiO_2 is to be deposited from a 0.1-cm thick quartz disc by conventional dc sputtering. For quartz, $\rho \approx 10^{16}$ Ω-cm. To draw a current density J of 1 mA/cm^2, the cathode needs a voltage $V = 0.1J\rho$. Substitution gives an impossibly high value of 10^{12} V, which indicates why dc sputtering will not work.

Now what happens when an ac signal is applied to the elctrodes is considered. Below about 50 kHz, ions are sufficiently mobile to establish a complete discharge at each electrode on each half cycle. Direct current sputtering conditions essentially prevail at both electrodes, which alternately behaves as cathodes and anodes. Above 50 kHz two important effects occur. Electrons oscillating in the glow region acquire enough energy to cause ionizing collisions, reducing the need for secondary electrons to sustain the discharge. Secondly, RF voltages can be coupled through any kind of impedence so that the electrodes need not to be conductors. This makes it possible to sputter any material irrespective of its resistivity. Typical RF frequencies employed range from 5 to 30 MHz.

However, 13.56 MHz has been reserved for plasma processing by the Federal Communications Commision and is widely used.

RF sputtering essentially works because the target self-biases to a negative potential. When this happens, it behaves like a dc target where positive ion bombardment sputters away atoms for subsequent deposition. Negative target bias is a consequence of the fact that electrons are considerably more mobile than ions and have little difficulty in following the periodic change in the electric field. The disparity in electron and ion mobilities means that isolated positively charged electrodes draw positive ion current.

However, since ac electricity is involved, sputtering occurs at both elctrodes which presents a potential problem because the resultant film may be contaminated as a consequence. For sputtering from only one electrode, the sputter target must be an insulator and be capacitatively coupled to the RF generator. The equivalent circuit of the sputtering system can be thought of as two series capacitors – one at the target sheath region, the other at the substrate – with the applied voltage divided between them. Since capacitive resistance is inversely proportional to the capacitance or area, more voltage will be dropped across the capacitor of a smaller surface area. Therefore, for efficient sputtering the area of the target electrode should be small compared with the total area of the other, or directly coupled, electrode. In practice, this electrode consists of the substrate stage and system ground, but it also includes baseplates, chamber walls, etc.

2.3.2.3.3 Magnetron Sputtering: Magnetic fields are used quite a lot in sputtering systems. They give advantages in sputtering rate and extendability of operating range, and can reduce electron bombardment at the substrate. The problem of uniformity that sometimes arise, can be overcome in many cases [20].

The primary interaction between a particle of charge q and velocity v, and a magnetic field B, is to produce a force on the particle of magnitude $F = Bqv$. The direction of the force is perpendicular to both the magnetic field and the velocity and is better expressed in the vector form:

$$\mathbf{F} = q\ \mathbf{v} \times \mathbf{B} \tag{2.23}$$

The force produces an acceleration that is inversely proportional to the mass of the charge. For the magnetic fields used in sputtering, which are typically 100 gauss, only the electrons are affected; the ions are too massive.

The purpose of using a magnetic field in a sputtering system is to make more efficient use of the electrons, and cause them to produce more ionization. In a conventional glow discharge, electrons are soon lost by recombination at the walls. To minimize this loss, there are two ways of using a magnetic field which are rather different in approach: (1) Parallel electric and magnetic fields and (2) Perpendicular electrical and magnetic field. The latter one will be discussed briefly because of its relevance with this research.

2.3.2.3.3.1 Electron Motion in Perpendicular Electric and Magnetic Field: In magnetrons, electrons ideally do not even reach the anode but are trapped near the target, enhancing ionizing efficiency there. This is accomplished by employing a magnetic field oriented parallel to the target and perpendicular to the electric field, as shown schematically in Fig. 2.5.

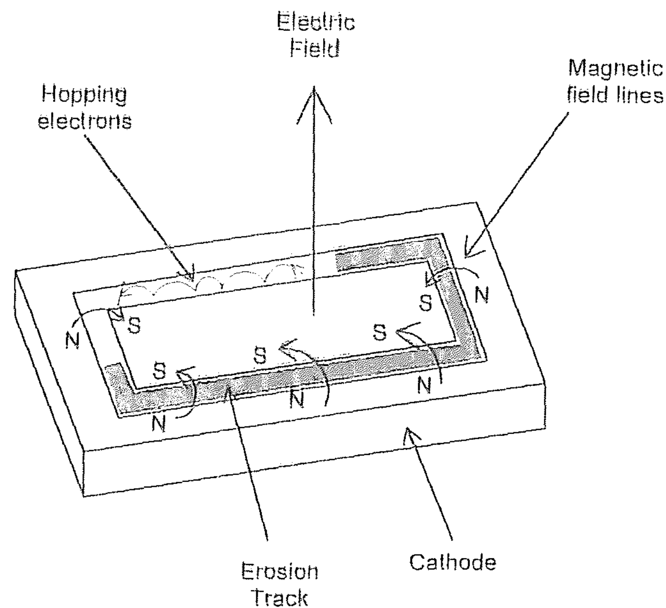

Figure 2.5: Applied fields and electron motion in the planar magnetron

Practically this is achieved by placing a bar or horse-shoe magnet behind the target. Therefore, the magnetic field lines first emanate normal to the target, then bend with a component parallel to the target surface (this is the magnetron component) and finally return, completing the magnetic circuit. Electrons emitted from the cathode are initially accelerated toward the anode, executing a helical motion in the process; but when

they encounter the region of the parallel magnetic field, they are bent in an orbit back to the target. By suitable orientation of target magnets, a "race track" can be defined where the electrons hop around at high speed. Target erosion by sputtering occurs within this track because ionization of the working gas is most intense above it.

Magnetron sputtering is presently the most widely commercially practiced sputtering method. The chief reason for its success is the high deposition rates achieved (e.g., up to 1 μm/min for Al). These are typically in order of magnitude higher than rates attained by conventional sputtering techniques. Popular sputtering configuration utilize planar, toroidal (rectangular cross-section), and toroidal-conical (trapezoidal cross section) targets.

2.3.2.3.4 Reactive Sputtering: In reactive sputtering, thin films of compounds are deposited on substrates by sputtering from targets in the presence of a reactive gas, usually mixed with the inert working gas (invariably Ar). The most common compounds reactively sputtered (and the reactive gases employed) are briefly listed [20]:

1. Oxides (oxygen)- Al_2O_3, In_2O_3, SnO_2, SiO_2, Ta_2O_5
2. Nitrides (nitrogen, ammonia)- TaN, TiN, AlN, Si_3N_4, C_3N_4
3. Carbides (methane, acetylene, propane)- TiC, WC, SiC
4. Sulfides (H_2S)- CdS, CuS, ZnS
5. Oxycarbides and oxynitrides of Ti, Ta, Al, and Si

Irrespective of which of these materials is considered, during reactive sputtering the resulting film is either a solid solution alloy of the target material doped with the reactive

element (e.g., $TaN_{0.01}$), a compound (e.g., TiN), or some mixture of the two. Westwood has provided a useful way to visualize the conditions required to yield alloys or compounds [21]. These two regimes are distinguished in Fig. 2.6, illustrating the generic hysteresis curve for the total system pressure (P) as a function of the flow rate of reactive gas (Q_r) into the system. The dotted line represents the variation of P with flow rate of an inert sputtering gas (Q_i). The solid line represents the similar relationship for reactive gas (in this case, for sputtering of Ta with Ar gas in presence of N_2). As Q_r increases from $Q_r(0)$, the system pressure essentially remains at the initial value P_o because N_2 reacts with Ta and is removed from the gas phase. But beyond a critical flow rate Q_r^*,

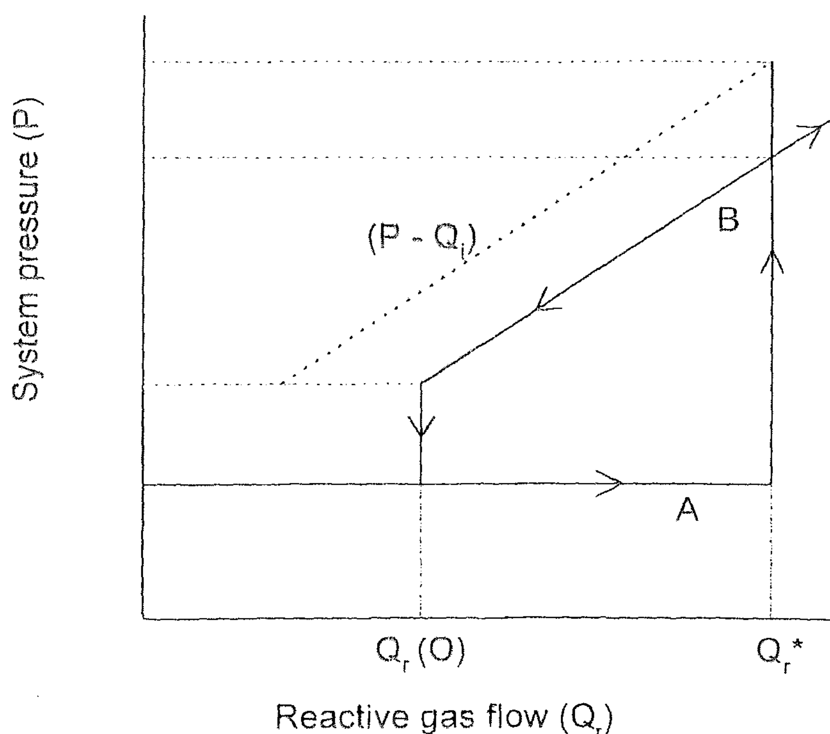

Figure 2.6: Generic hysteresis curve for system pressure vs. reactive gas flow rate during reactive sputtering

the system pressure jumps to the new value P_1. If no reactive sputtering took place, P would be somewhat higher (i.e., P_3). Once the equilibrium value of P is established, subsequent changes in Q_r cause P to increase or decrease linearly as shown. As Q_r decreases sufficiently, P again reaches the initial pressure.

The hysteresis behavior represents two stable states of the system with a rapid transition between them. In state A there is little change in pressure while for state B the pressure varies linearly with Q_r. Clearly, all of reactive gas is incorporated into the deposited film in state A- the doped metal and the atomic ratio of reactive gas dopant to sputtered material increases with Q_r. The transition from state A to state B is triggered by compound formations on the metal target.

The choice of whether to employ compound targets and sputter reactively is not always clear. If reactive sputtering is selected, then there is the option of using simple dc diode, RF, or magnetron configurations. The choice depends on many factors including: target purity, deposition rates, stoichiometry and properties of deposited films.

2.3.2.4 Evaporation vs. Sputtering: Relative advantages and disadvantages of evaporation and sputtering processes are listed in Table 2.1.

Table 2.1 Evaporation vs. Sputtering

	Evaporation	Sputtering
A. Production of Vapor Species		
1.	Thermal evaporation mechanism	Ion bombardment and collisional momentum transfer.
2.	Low kinetic energy of evaporant atoms (at 1200 K, E = 0.1 eV)	High kinetic energy of sputtered atoms (E=2-30 eV).
3.	Directional evaporation according to cosine law	Directional sputtering according to cosine law at high sputter rate.
4.	Fractionation of multi-component alloys, decomposition, and dissociation of compounds	Generally good maintenance of target stoichiometry.
5.	Availability of high evaporation source purities	Sputter target of all materials are available; purity varies with material
B. The Gas Phase		
1.	Evaporant atoms travel in high or ultrahigh vacuum ($\sim 10^{-6} - 10^{-10}$ torr) ambient.	Sputtered atoms encounter high pressure discharge region (~ 100 mtorr).
2.	Thermal velocity of evaporant 10^5 cm/sec.	Neutral atom velocity ~ 5×10^4 cm/sec.
3.	Mean-free path is larger than evaporant-substrate spacing. Evaporant atoms undergo no collisions in vacuum.	Mean-free path is less than target-substrate spacing. Sputtered atoms undergo many collisions in the discharge
C. The Condensed Film		
1.	Condensing atoms have relatively low energy.	Condensing atoms have high energy.
2.	Low gas incorporation.	Some gas incorporation.
3.	Few grain orientation (textured films)	Many grain orientation.
4.	Grain size generally larger than for sputtered films (epitaxy possible).	Good adhesion to substrate

2.3.3 Hybrid and Modified PVD Processes

Other than conventional evaporation and sputtering processes, there are several more complex PVD processes, which demonstrate the diversity of process hybridization and modification possible in producing films with unusual properties. Ion plating, reactive evaporation, ion-beam-assisted deposition, and ionized cluster beam deposition are the processes included in this category. Because of relevance with this study, only ion-beam-assisted deposition will be introduced briefly in this section.

2.3.3.1 Ion-Beam-Assisted Deposition Processes: Ion bombardment of biased substrates during sputtering is a particularly effective way to modify film properties [20]. Process control in plasma is complex due to the difficulties to regulate the direction, energy, and flux of the ions incident on the growing film. Ion-beam-assisted processes are capable to provide independent control of the deposition parameters and, particularly, the characteristics of the ions bombarding the substrate. Two main ion source configurations are employed. In the dual-ion-beam system, one source provides the inert or reactive ion beam to sputter a target in order to yield a flux of atoms for deposition onto the substrate. Simultaneously, the second ion source, aimed at the substrate, supplies the inert or reactive ion beam that bombards the depositing film. Separate film-thickness-rate and ion-current monitors, fixed to the substrate holder, enable the two incident beam fluxes to be independently controlled.

In the second configuration, an ion source is used in conjunction with an evaporation source. The process known as ion-assisted deposition (IAD), combines the

benefits of high film deposition rate and ion bombardment.

Broad-beam (Kaufman) ion sources, the heart of ion-beam-assisted deposition systems, has been optimized to yield high-ion-beam fluxes for given power inputs and gas flows. Current densities of several mA/cm^2 are achieved ($1\ mA/cm^2$ is equivalent to 6.25×10^{15} ions/cm^2-sec or several monolayers per second). The resulting beams have a low-energy spread (typically 10 eV) and are well collimated, with divergence angle of only a few degrees. Furthermore, the background pressure is quite low ($\sim 10^{-4}$ torr) compared with typical sputtering or etching plasmas.

2.4 Film Formation Mechanism

In physical vapor deposition, material arrives at the substrate mostly in an atomic or molecular form. The atom diffuses around the substrate with a motion determined by its binding energy to the substrate and influenced by the nature of the substrate. The surface of the substrate offers adsorption sites for the depositing and diffusing atoms. After certain time, adatoms either evaporate from the surface or join with another adjacent single atom to form doublet. The process continues to form triplet, quadruplets and so on. This is the nucleation stage of thin film growth, leading to the formation of quasi-stable islands. These islands grow in size rather than in numbers, coalesce with each other and coalescence proceeds until the film reaches continuity. These steps are shown schematically in Fig. 2.7.

(a) Single atom arrives

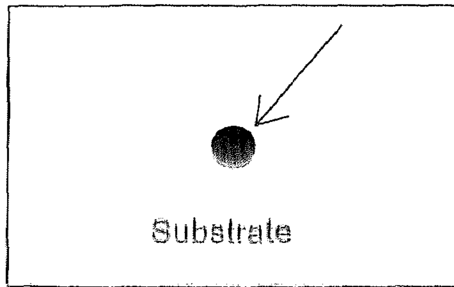

(b) Migration Re-evaporation

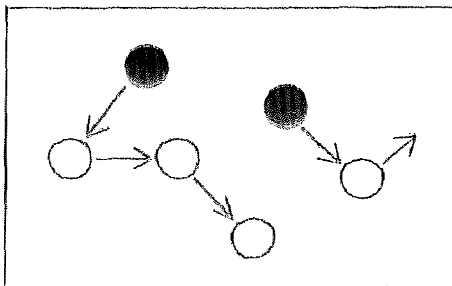

(c) Collision and combination of single atoms

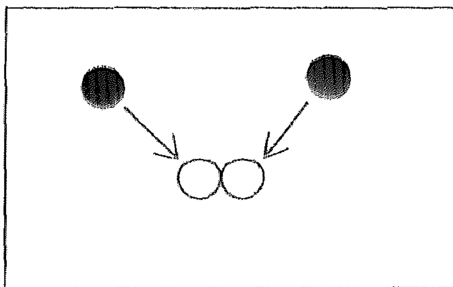

(d) Nucleation

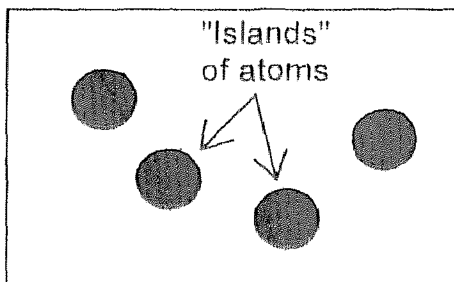

(e) Island Growth

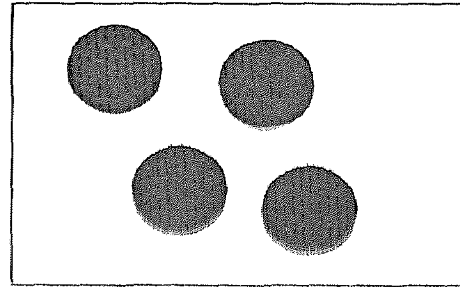

(f) Island shape

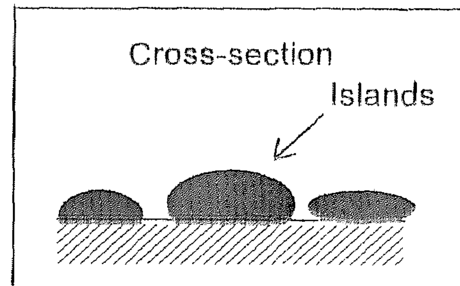

(g) Coalescence

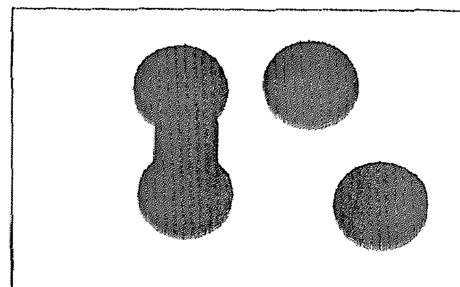

(h) Continuity

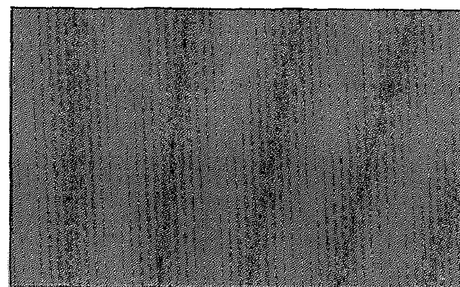

Figure 2.7: Formation of a thin film

CHAPTER 3

REVIEW OF LITERATURE

Ever since Liu and Cohen [2-4] published their modeling results which predicted β-C_3N_4 to have super-hardness, many attempts were made to produce this hypothetical material [5-19][22-28]. A successful synthesis of the homogeneous crystalline state of β-C_3N_4 with desired bonding has not been reported yet. In this section, major technical difficulties in synthesis of carbon nitride thin solid films will be addressed followed by a brief discussion on the success to date to deposit β-C_3N_4 reported in literature.

3.1 Technical Barrier to Synthesize Carbon Nitride Thin Film

1. As observed in the formation of all other nitride systems, effective nitrogen incorporation is the first technical barrier. Poor nitrogen incorporation using N_2 (or NH_3) gases or conventional nitrogen plasma sources is due to the ineffective dissociation of nitrogen molecules, which in turn does not provide sufficient reactive atomic nitrogen at the growth surface. The energy needed to dissociate and excite nitrogen is several times higher than that used in typical plasmas.
2. Carbon nitride has a very high cohesive energy (81 eV per unit cell) and, similar to diamond, is a metastable structure. The proper bonding structure between carbon and nitrogen in β-C_3N_4 is found to be C-N, sp^3 hybridized sigma bond. Thus, control of energy of reactive species is the most crucial step to synthesize carbon nitride with desired bonding.

3.2 Results to Date to Synthesize β-C_3N_4

Since carbon nitride appears to be similar in bonding energy and thermodynamics to diamond, established technical approaches to synthesize diamond were investigated to synthesize carbon nitride film. The high pressure, high temperature technique to produce artificial crystalline diamond fails to form carbon nitride for several reasons. The theoretical thermodynamic data for carbon nitride is not established yet due to the fact that the carbon nitride is a binary system and it is much more complicated than that of diamond. It is difficult to predict the conditions for the preferential formation of carbon nitride since there are at least 5 important synthesis variables (temperature, pressure, concentration of nitrogen, concentration of carbon, and other reactant present). Attempts using this approach generally produce polymers, graphite or diamond [8][10, 11].

Attempts using different types of CVD techniques with the aid of atomic hydrogen reveal that atomic hydrogen does not have a catalytic effect in formation of carbon nitride although it catalyzes sp^3 carbon-carbon bond formation in diamond synthesis [7][29-32].

Attempts using energetic vapor phase deposition have shown some success in the formation of the carbon nitride. For the case of diamond formation, the optimum energy window was found to be 70-80 eV. The ratio of sp^3 to sp^2 bonds in diamond was found to be 30-40%, 70%, and 90% for sputtering, laser ablation, and plasma arc respectively. Tompa et al.[33] showed that the optimum energy window for the formation of amorphous, hard carbon nitride is ~ 150 eV. But none of the conventional vapor phase deposition techniques have their mean energy in the 150 eV range.

The published work can be categorized as to the number and amount of the carbon nitride phases found in the films synthesized by different methods and analyzed by a variety of techniques (XPS, TEM, RBS, Raman Spectroscopy, FTIR and so on) [34-43]. Rabalais et al. [34] generalized the XPS results obtained from carbon nitride samples deposited by three different techniques (ion beam deposition, ECR plasma assisted e-beam evaporation, and dc magnetron sputtering) [34][41-43]. The researchers claimed all the films having a similar composition consisting of two phases. One phase had a stoichiometry near C_3N_4 and was identified as a tetrahedral compound. The other phase had a variable stoichiometry from C_5N to C_2N and was identified as predominantly sp^2 bonded structure. However, a group based at the Macquarie University in Australia [38] has opposed the two-phase structural model suggested by Rabalais et al. [34][41][42]. They emphasized that the carbon nitride films with high nitrogen content (grown by Rabalais et al. [34]) exhibit high electrical resistivity and as a consequence, XPS results are likely not to be accurate due to sample charging effects during measurements unless special precautions are taken. Kumar et al. deposited carbon nitride films by radio frequency reactive magnetron sputtering of graphite in pure nitrogen plasma and analyzed them by XPS [34]. They reported at least three different types of bonding present in the film, C-N single bond, C≡N triple bond, and C-N bond similar to the bond in graphitic C-C.

Fernandez et al. investigated electron energy loss spectra of carbon nitride films synthesized by dual ion beam sputtering [44]. Their study suggests that C in C=N bond is sp^2 hybridized. Additionally, the analyses of the TEM diffraction patterns indicated the

formation of β-C_3N_4 crystallites embedded in a layer of polymeric CN_x amorphous phase [44]. A maximum value of N/C = 0.8 (44 at% of nitrogen) has been achieved in that work. Similar results have also been claimed by Riviere et al. [40].

Recently, Hammer et al. [39] have reported interesting data on a chemical reaction between carbon and nitrogen which leads to formation of a volatile chemical compound. In their approach, the carbon nitride films were synthesized by ion beam assisted sputtering, where a graphite target was sputtered by argon or nitrogen plasma and the growing film was simultaneously bombarded by a focused nitrogen beam of energies between 100-800 eV at 100 and 400 ^oC. It has been found that the growth occurs only if the ion to atom arrival ratio I/A is smaller than a critical value of about 1.8 and it appears to be almost independent of the assisting beam energy.

In China, Wu et al. presented the results of XPS analysis suggesting co-existance of different carbon phases, tetrahedrally bonded phase β-C_3N_4 and other carbon nitrides (the ratio of N/C varied from 0.5 to 1.1)[45]. In another study, Zhang et al. claimed the formation of crystalline carbon nitride films by RF plasma assisted CVD [46]. They identified the XRD peaks similar to those predicted theoretically for crystalline carbon nitride. However, this claim was not supported by additional evidence.

Kreider et al. of NIST produced amorphous carbon nitride coatings containing up to 40% nitrogen using planar magnetron RF sputtering in a nitrogen atmosphere [47]. Films with transparency greater than 95% in the visible wavelength and harder than silicon have been produced.

Tompa and Murzin reported some promising results to synthesize carbon nitride films by negative ion beam assisted deposition (NIBAD) and reactive magnetron sputtering [12][33]. They found that use of nitrogen ion beam during the film growth, either by NIBAD or by magnetron sputtering results in the formation of a triple stretching C≡N bond. The films generated by both methods are similar in that they consists of a mixture of C=C, C≡N bonds incorporated in predominantly sp^2 hybridized network of variable size aromatic rings, with their planes cross-linked by sp^3 hybridized bonds. They were the first to report that for the NIBAD films, lowering of carbon energy leads to formation of graphitic domains growing in size and/or number. However, FTIR and Raman have not confirmed the presence of a crystalline β-C_3N_4. The nitrogen concentration in their film was calculated to be near 50% by AES.

Most recently, a group of Chinese researchers claimed formation of α- and β-carbon nitride as well as other unidentified phases in bulk quantities by hot filament CVD and an ion-beam assisted method [16-19]. A summary of literature review is given in Table 3.1

Table 3.1 The Summary of Results on Synhesis of Carbon Nitride Obtained Worldwide

Organization / Person	Approach	Results	Reference
Sproul et al., Northwestern University, USA	Reactive ionized and unbalanced sputtering	Amorphous CN_x with small crytallites	[51, 52, 54]
Rabalais et al., University of Houston, USA	Ion beam deposition	Mixture of graphitic carbon and triply bonded CN	[3, 47, 48]
Sundgren, Linkoping University, Sweeden	Reactive Sputtering	Microhardness of 40-60 GPa	[58]
Lieber et al., Harvard University, USA	Laser ablation and ion bombardment	Mixture of single, double and triple bonded CN	[63]
Krieder et al., NIST, USA	Ion bombardment reactive sputtering	40% Nitrogen & 95% transparent films	[61]
Tompa & Murzin, SMI, USA	NIBAD and reactive magnetron sputtering	The first to report the sp^2/sp^3 Raman intensities ratio dependencies on C ion energy and N ion current.	[11, 12]
Fernandez et al., Spain	IBAD	Small crystallite of C_3N_4 embedded in a layer of polymer-like amorphous CN_x	[46]
Riviere et al., France	Ion beam sputtering	50-100 nm sized crystallites of C_3N_4 by TEM and RBS	[10]
Zhang et al., China	rf- assisted CVD	Crystalline beta-C_3N_4	[50]
Wu et al., China	High dose ion implantation	Co-existance of different C phases, tetrahedrally bonded phase β-C_3N_4 and other CN phases (ratio of N/C varied from 0.5 to 1.1)	[49]

Table 3.1 The Summary of Results on Synhesis of Carbon Nitride Obtained Worldwide (Continued)

Chen et al., China	Hot filament CVD	Co-existance of crystalline α-, and β-C_3N_4 with other unidentified phases.	[16-19]

CHAPTER 4

EXPERIMENTS

4.1 Introduction

Carbon nitride thin solid films were synthesized using radio frequency reactive magnetron sputtering. Performance of a Cs enhanced negative carbon ion source was also studied to investigate synthesis of carbon nitride film by negative ion beam assisted deposition. Plasma characteristics of the process were investigated at various deposition process parameters including RF power, gas composition and chamber pressure. Scratch resistance of the films was evaluated using scratch test. Young's modulus and hardness of the films were measured by using nano hardness tester. Film structure was evaluated by Raman spectra analysis.

4.2 Sputtering System

The schematic of the sputtering system used to synthesize carbon nitride thin film is presented in Fig 4.1. The system consists of a high vacuum vertical stainless steel chamber of 18 inches in diameter and 15 inches in height. The interior of the chamber can be reached by removing the top plate of 22 inches in diameter. The chamber is sealed at top end with a viton O ring. Three HPS type pirani pressure gauges were used to measure pressure with a range of atmospheric to 10^{-4} Torr at different location of the system. A dual-filament, nude ionization gauge with a range from 10^{-4} to 10^{-9} Torr was

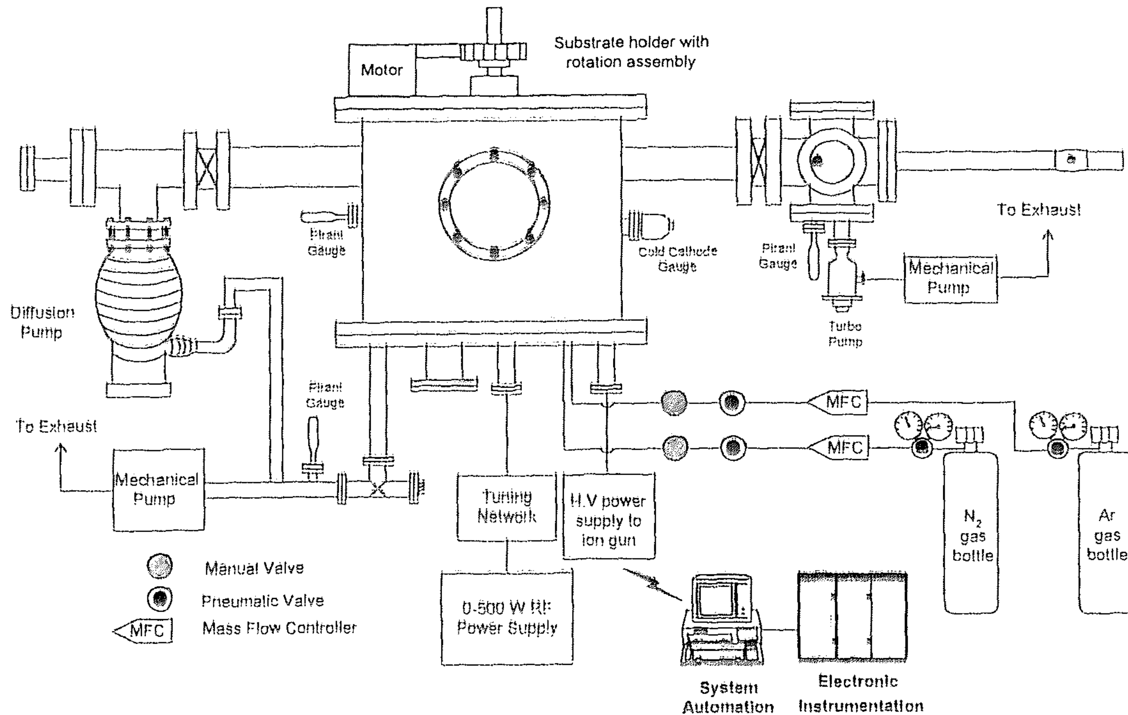

Figure 4.1: Schematic of carbon nitride thin film deposition system

used to measure the base pressure inside the chamber. Pressure reading of pirani gauges were displayed by a HPS 937 type gauge controller. A Granville-Phillips 307 type vacuum gauge controller displayed the reading of ionization gauge. The system was equipped with two vacuum-sealed gas inlet. MKS type mass flow controllers and pneumatic valves controlled the flow rates of argon and nitrogen gases into the chamber.

The system was kept at low pressure by vacuum pumps. A series combination of an Edward 80 type two stage rotary mechanical pump and a Varian VHS M6 type diffusion pump was used to achieve a vacuum inside the chamber as low as 10^{-6} torr. The system was equipped with a load lock to facilitate transfer of sample without disturbing

disturbing the vacuum of the chamber. A separate series combination of an Edward 18 type two stage rotary mechanical pump and a Varian turbo-V 80 type turbo-molecular was used to achieve a vacuum inside the load lock comparable to that inside the chamber. A 4.5 inches in diameter manual gate valve was used between chamber and load lock to isolate one from the other. Another 8 inches in diameter manual gate valve was used between chamber and diffusion pump to control chamber pressure for a fixed flow rate of sputtering gas.

A two-inch diameter ONYX-2 magnetron sputtering gun (manufactured by Angstrom Science, Inc.) was used to hold and sputter a two-inch diameter 99.99% pure graphite target in presence of plasma. The sputtering gun was powered by a RFX-600 type (manufactured by Advanced Energy) RF power supply which was capable of supplying 0-500 W RF power at 13.56 MHz frequency. An ATX-600 type matching network (manufactured by Advanced Energy) was used to match the impedence of the plasma for zero reflected power condition. The system was also equipped with a 3-cm diameter Kaufman ion source (manufactured by Ion Tech, Inc.) capable of producing 50-500 eV N_2 ion beams. The operation of the ion beam was controlled by a MPS-3000FC type (Ion Tech, Inc.) controller. A STM-100/MF type (Sycon Instruments) quartz monitor was used for in situ monitoring of deposition rate and film thickness.

The system was capable of providing substrate rotation at a constant speed of 1-5 rpm by an electrically isolated Ferrofluidics™ feedthrough. A computer based control system was used to control the deposition condition including flow rate of gases, substrate rotation speed.

4.3 Negative Carbon Ion Souce

Fig. 4.2 illustrates the cross-sectional schematics of the cesium enhanced negative carbon ion source.

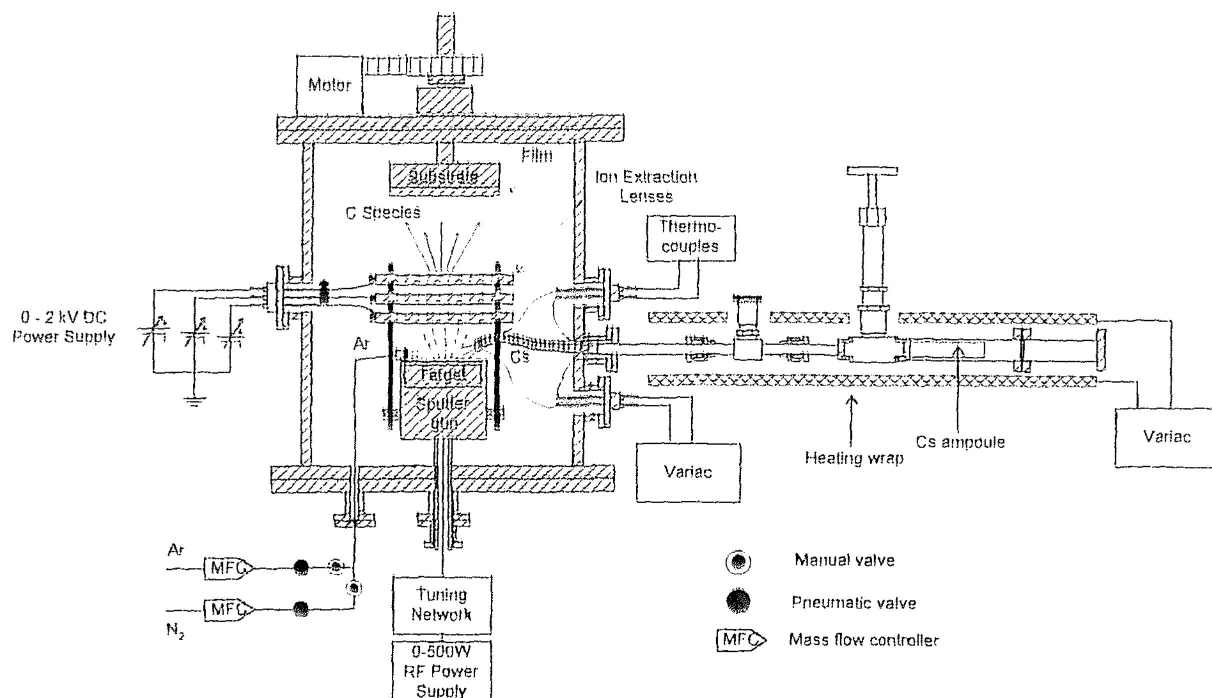

Figure 4.2: Cross-sectional schematic of a negative carbon ion source

The system consists of a cesium atomic flux oven (designed and manufactured by SMI, Inc.)[48][49] and three Einsel lenses held on top of the sputtering gun with an aluminium ring and four ceramic rods. Hence, the lenses were electrically isolated from the sputter gun. The cesium oven was built similarly to the one described in [48]. Its function was to supply an atomic flux of evaporated cesium to the sputter gun head. Generally, after a cesium ampoule was introduced into the oven, it was pumped down and

then heated up to operation temperature (200-275°C) with the heating tape wrapped around the atmospheric part of the oven and the custom made wire-wrap heater in vacuum. Temperature controllers monitor the temperature at different part of the oven and the temperature of the transport line was usually kept at a temperature higher than the portion enclosing the cesium ampoule. The in-vacuum cesium transport line was essentially flexible tubing aimed at the carbon sputter target mounted on the top of the sputter gun.

4.4 Deposition Procedure

4.4.1 Leakage Check

A leak would result in a change in the deposited structure (due to oxygen). Again a cleaner and better vacuum is required for PVD processes. Therefore leak checking in PVD systems is an important step before making an experiment. When leakage check was carried out, all pneumatic controllers and gas delivery valves were fully open to the gas cylinder main valve. After pumping the system for a whole day, closing the outlet gate valve of the chamber, the rate of pressure increase was measured for a fixed period of time in the chamber to obtain the leakage rate. For the system under study, the leakage rate was approximately 10^{-6} Torr/sec.

4.4.2 Loading Substrate

Substrates were loaded inside the chamber by using a load lock. A load lock consists of a horizontally movable stainless steel rod with a provision of holding the substrate at one

end. The Load lock was pumped down after loading the substrate into it. When the vacuum reached comparable to that inside the chamber, the manual gate valve was opened and the substrate was placed on the substrate holding platform of the chamber. The substrate holder platform was horizontal and it was connected to the top plate of the chamber and was placed at about four and half inch below the top plate. Unloading of the substrate was done in the opposite way. The load lock was brought to atmospheric pressure by opening the vent port before taking the sample out. Films were deposited on <111> oriented single sided, polished silicon wafers of two inches in diameter.

4.4.3 Deposition

Once the required base pressure was reached and leakage check was done, wafer was bombarded with a 500 eV, 10 mA nitrogen ion beam for 5 minutes to clean the surface from any particle loosely bonded to it. Then the chamber was back filled with argon using 10-15 sccm of Ar. The plasma was ignited at 25-30 watts of RF power at a chamber pressure of 13-20 mTorr. Once the plasma was ignited, reducing Ar gas flow rate to 4-5 sccm reduced the chamber pressure to 2-5 mTorr. No deposition was observed at such low power levels. Exposing the substrate to low power plasma for a few minute was observed to be advantageous for further cleaning of the substrate. Nitrogen was introduced at this stage according to the deposition condition. The RF power was raised slowly to the deposition power and the time of deposition was monitored. Film thickness was dependent on deposition time.

4.5 Characterization of Carbon Nitride Thin Films

4.5.1 Scratch Resistance

The film scratch resistance was measured by MST-CSEMEX® micro scratch tester. The scratch-test method consists of generating scratches with a spherical stylus (Rockwell C diamond, tip radius 200 μm) which was drawn at a constant speed of 10 mm/min across the coating-substrate system and at progressive loading rate of 1 N/min. For progressive loading, the critical load (Lc) was defined as the smallest load at which a recognizable failure occurs.

The driving forces for coating damage in the scratch test were a combination of elastic-plastic indentation stresses, frictional stresses, and the residual internal stresses. The equipment detected elastic waves generated as a result of the formation and propagation of microcracks, and the corresponding load at which acoustic emission was detected gave the critical load for failure. Five scratch tests were performed on each sample and the value of critical load was taken as the average of all five values.

4.5.2 Hardness and Young's Modulus

The hardness and Young's modulus of the films deposited were measured using CSEM-NHT type nano-hardness tester. The nano-hardness tester was capable of measuring a maximum displacement of 10 μm at a displacement resolution of 1 nm and applying a maximum force of 40 mN at a force resolution of 10 μN. The measurement was performed with a Vickers diamond No. 1 type indenter with a maximum force of 3 mN at a loading rate of 6 mN/min.

The equipment used an already established method where an indenter with a known geometry was driven into a specific site of the sample, by applying an increasing normal load. When reaching a preset maximum value, the normal load was reduced until partial or complete relaxation occurred. This procedure was performed repetitively; at each stage of the experiment the position of the indenter relative to the sample surface was precisely monitored with a differential capacitive sensor.

For each loading/unloading cycle, the applied load value was plotted with respect to the corresponding position of the indenter. Using unloading data, mathematical relationship best suited for the indenter geometry, and area function, parameters such as contact depth h, stiffness S and projected contact area were determined. The reduced modulus, E_r, is given by:

$$E_r = \frac{S\sqrt{\pi}}{2\sqrt{A_c}} \tag{4.1}$$

The Young's modulus, E, can then be obtained from:

$$\frac{1}{E_r} = \frac{1-v^2}{E} + \frac{1-v_i^2}{E_i} \tag{4.2}$$

And hardness was determined from the maximum load, P_{max}, divided by the projected contact area:

$$H = \frac{P_{max}}{A_c} \tag{4.3}$$

4.5.3 Raman Scattering

Structural properties of the films were evaluated by Raman scattering analysis. A 5 W Lexel Ar ion laser operating at 514.5 nm excited the Raman scattered light with approximately 375 mW incident on the sample. A 514.5 nm band pass filter eliminated the plasma lines from the primary laser line. A combination of a dielectric laser mirror and a cylindrical lens directed the laser onto the sample in a backscattered geometry. The scattered light was focused into a double grating SPEX 1401 double spectrometer using two optical lenses in series. A Product for Research Photomultiplier tube (PMT) was used to detect the scattered light. A Stanford Research SR445 type amplifier and a SR-400 type two channel gated photon counter were used to analyze the photo-current from the PMT. A computer controlled and stored the data for post processing.

Local bonding properties of the film can be obtained from Raman absorption bands. Raman data shows a variety of signals which must be understood in order to evaluate film properties since there are no standard for hypothetical metastable carbon nitride.

The optic-phonon branch frequency can be expressed as below for a 2-atom unit cell [50]

$$w^2 = 2C\left[\frac{1}{M_1} + \frac{1}{M_2}\right] \tag{4.4}$$

where M_1 and M_2 are effective mass of each atoms, and C is the bonding force constant.

CHAPTER 5

RESULTS AND DISCUSSIONS

5.1 Introduction

The results of plasma characteristics, performance evaluation of cesium enhanced negative carbon ion source and carbon nitride thin films deposited on Si wafers mostly at 300 watts and at various Ar-N_2 gas composition at 5 mTorr pressure are presented in this chapter.

5.2 Plasma Characteristics

The purpose of this study was to understand the behavior of deposition condition in terms of deposition rate and flux of charged species toward the substrate at different process parameters such as RF power, chamber pressure, and nitrogen composition in Ar-N_2 gas mixture. Deposition rate in glow discharge processes depends not only on the number of sputtered and reactive species present but also on the energy of species involved and the environment through which those species have to diffuse toward the substrate. Fig. 5.1 represents chamber pressure dependence of deposition rate at different RF power. The experiments were carried out with pure Ar gas at 75, 125, and 200 watts of RF power for a pressure range of 1.8 to 18 mTorr. Figure 5.1 shows that deposition rate increases with RF power since ionization of Ar gas atoms increases at higher power which in turn increases sputtering rate of carbon atoms. Again at each RF power, deposition rate decreases with increasing pressure because at higher pressure sputtered atoms collide

with larger number of gas molecules present in the plasma and some of them get thermalized before reaching the substrate. However, pressure effect was found to be less pronounced upto about 4 mTorr.

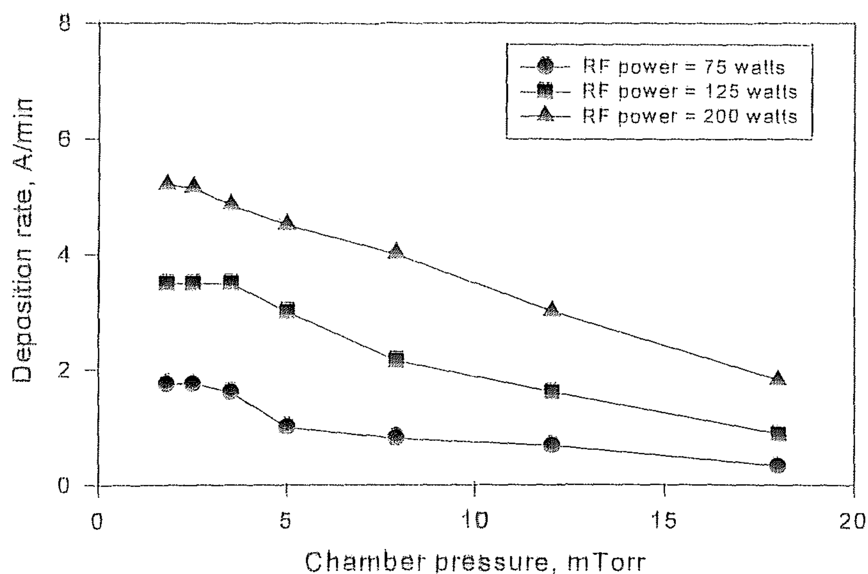

Figure 5.1: Variation of deposition rate with chamber pressure (with pure Ar plasma).

In Fig. 5.2, current absorbed at the substrate as measured by a digital multimeter during the experiment of deposition rate analysis is shown against chamber pressure for different RF power. Absorbed current is a measure of flux of charged species reaching the substrate during deposition. It was found that at lower RF power, absorbed current was almost unaffected by pressure. Higher the pressure, higher was the number of atoms or molecules present in the plasma. But this larger number of ionized species again undergo a higher degree of collision with other ions or gas species. These two opposing

effect counterbalance each other. However, at higher RF power, ions are more enrgetic and most of them can reach the substrate even though they experience higher collision at higher pressure. Again at higher pressure number of charged species also increases. So at higher RF power, current absored at the substrate was found to increase moderately with pressure.

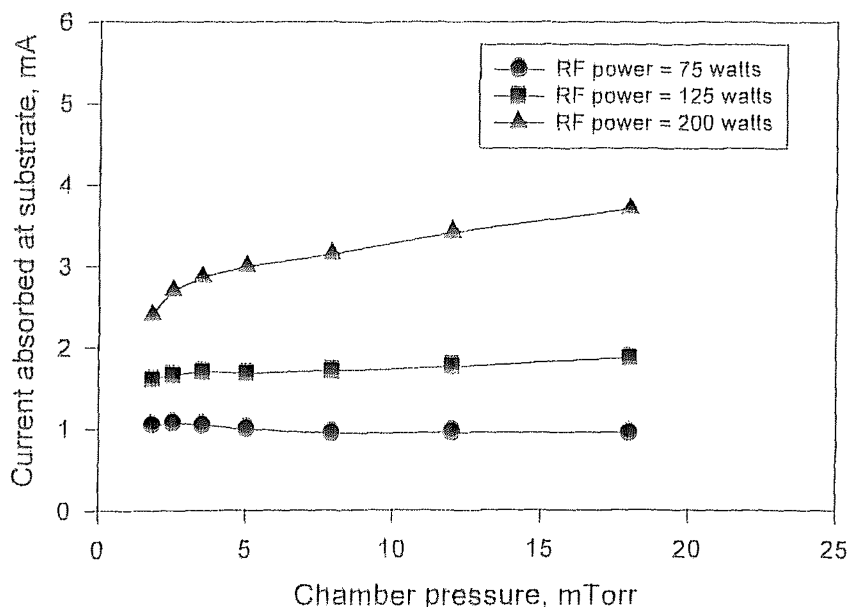

Figure 5.2: Variation of current absorbed at the substrate with chamber pressure at different RF power (with pure Ar plasma).

The effect of nitrogen composition in the Ar-N_2 gas mixture on deposition rate and current absorbed at substrate was also investigated at RF power of 150 Watts and is shown in Fig. 5.3. It is very interesting to note that, deposition rate and current absorbed at the substrate showed almost similar but opposite dependence with percentage of nitrogen in the Ar- N_2 plasma. Deposition rate increases with higher composition of

nitrogen probably due to abundance of atomic reactive nitrogen. Again higher atomic nitrogen means less ionic nitrogen and since Ar composition was lesser at higher nitrogen composition so the presence of Ar ions were also less. As a consequence of these two effects, absorbed current was observed to decrease with higher nitrogen composition. This explanation was also supported by the fact that Ar-N_2 plasma was not able to sustain for nitrogen composition higher than 60% is probably due to insufficiency of ions in the plasma.

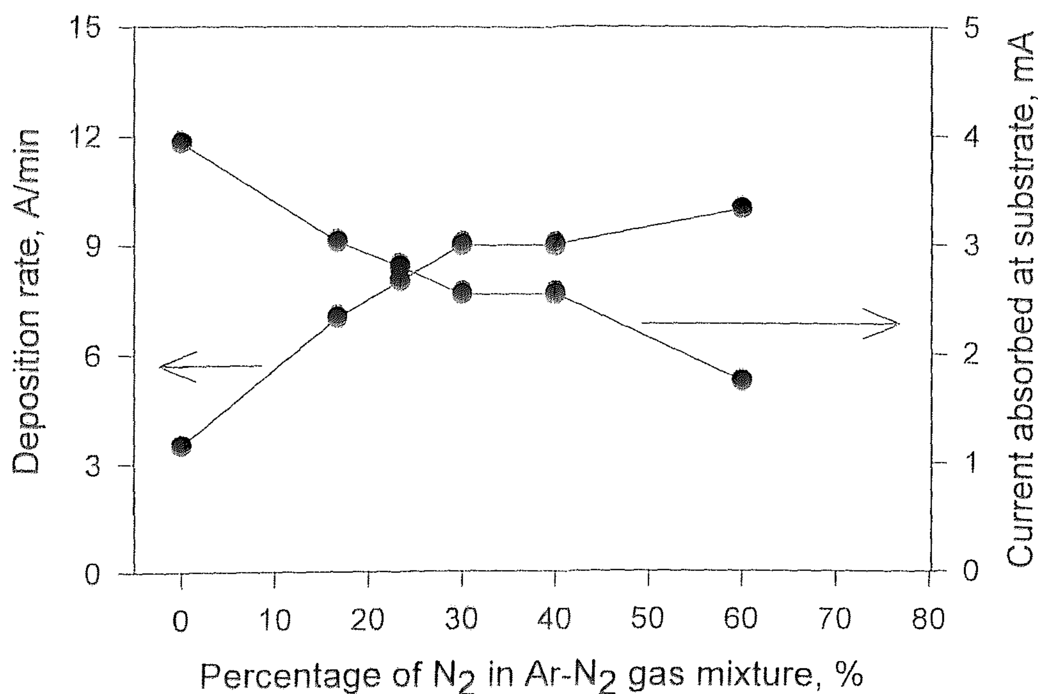

Figure 5.3: Variation of deposition rate and current absorbed at the substrate with nitrogen composition in Ar-N_2 gas mixture (at 150 W and 5 mTorr pressure).

A hysteresis plot for reactive sputtering of carbon with nitrogen is shown in Fig. 5.4. The straight line on the top represents chamber pressure dependence on flow rate of Ar gas at 150 watts. The graph on the bottom shows variation of chamber pressure with nitrogen flow rate at the same RF power and with a constant Ar gas flow of 5 sccm. Nitrogen flow rate was increased at steps of 0.5 sccm. However, no sudden pressure rise followed by a steady increase or decrease of pressure with increasing or decreasing flow rate of nitrogen was observed as it is usually observed in reactive magnetron sputtering of a metallic target (Fig. 2.6).

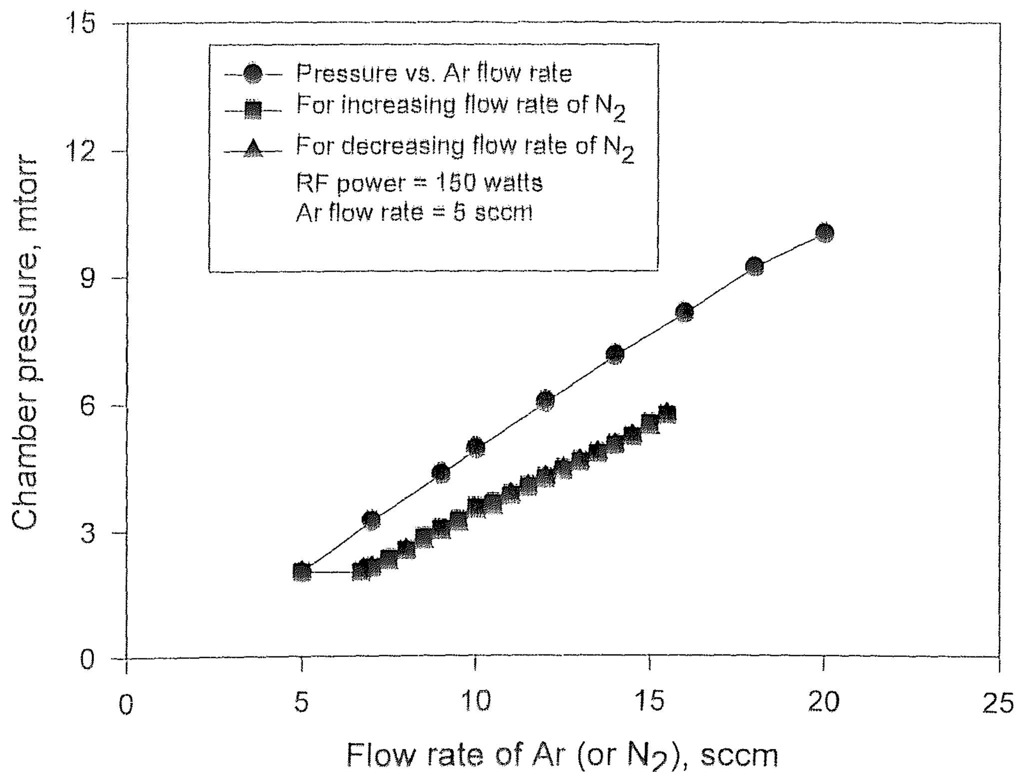

Figure 5.4: Hysteresis plot for recative sputtering of carbon with Ar-N_2 plasma.

5.3 Characterization of Films

Mechanical properties of the film, such as scratch resistance, microhardness, and Young's modulus, were evaluated for films synthesized at different compositions of nitrogen in the Ar-N_2 gas mixture. All films were synthesized at 300 watts RF power and the average thickness of the films were around 40 nm. Fig. 5.5 shows the variation of scratch resistance properties of the film with percentage of nitrogen in the Ar-N_2 gas mixture.

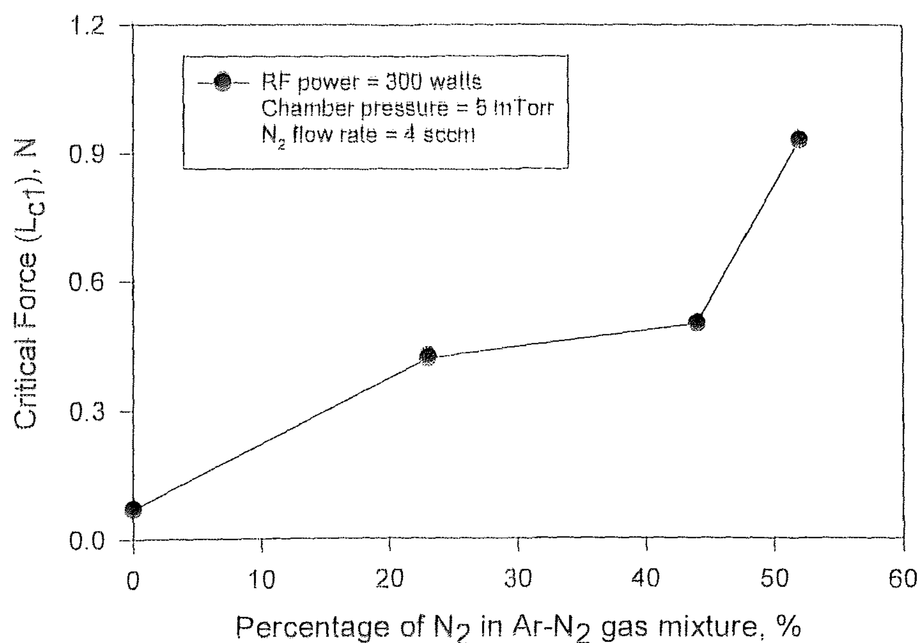

Figure 5.5 Variation of critical force with nitrogen composition in Ar-N_2 plasma.

The critical force at which first scratch occured was found to increase steadily with nitrogen composition in the Ar-N_2 plasma up to about 43 percent, however, a sharp increase in critical force was observed for nitrogen composition increasing from 43 to 52

percent. Critical force increased from 0.07 N for DLC film deposited with pure Ar plasma to a maximum value of 1 N for a film deposited with 53% nitrogen in Ar-N_2 plasma. Dependency of microhardness of the films with the same process parameter (% of nitrogen in Ar-N_2 plasma) is shown in Fig. 5.6.

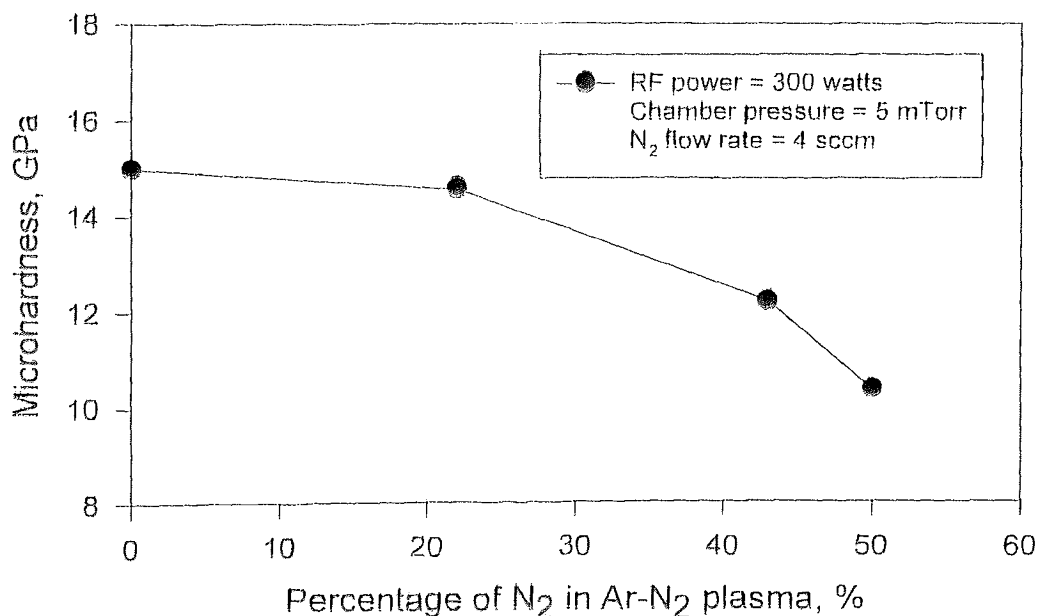

Figure 5.6 Variation of Microhardness of the film with N_2 composition in Ar-N_2 plasma.

Microhardnes of the film was observed not to change substantially with nitrogen composition of upto 23 percent and then decrease substantially. It is clear from Fig. 5.6 that the hardness of the film was not higher than that of a diamond like carbon film with a typical hardness of 15 GPa (point for 0% nitrogen) deposited at the same deposition

condition but moderately harder than the Si substrate with a hardnes of 6.5 GPa for bulk silicon[1].

Fig. 5.5 and 5.6 together suggests that higher nitrogen composition in plasma can improve the scratch resistance property of the film but can not improve hardness. Scratch resistance usually increases if there are comperatively fewer number of incomplete bonds or broken bonds. In this case, carbon atom should utilize its unpaired electrons to form bonds with other carbon and/or nitrogen atoms to increase scratch resistance property. The author believes that, higher nitrogen content provide sufficient reactive nitrogen at high RF power of 300 watts which can enhance bond formation between carbon and nitrogen. But hardness depend on how the bonding atoms are arranged in three dimensions. More speciafically hardness depends on the extent to which tetrahedral sp^3 bonds forms during deposition. It can be inferred that higher nitrogen content enhance bond formation but those bonds may not be tetrahedral sigma bonds which would contribute to the hardness of the film. This explanation can be supported by the Raman spectra analysis of the deposited films later in this section.

Fig. 5.7 shows the variation of Young's modulus of the films with nitrogen composition in Ar-N_2 plasma. Young's modulus was observed to decrease from 132.5 GPa to 130 GPa with composition of nitrogen from zero percent to 22 percent. Then young's modulus increased to a maximum value of 141 Gpa for 53 percent of nitrogen in Ar-N_2 plasma.

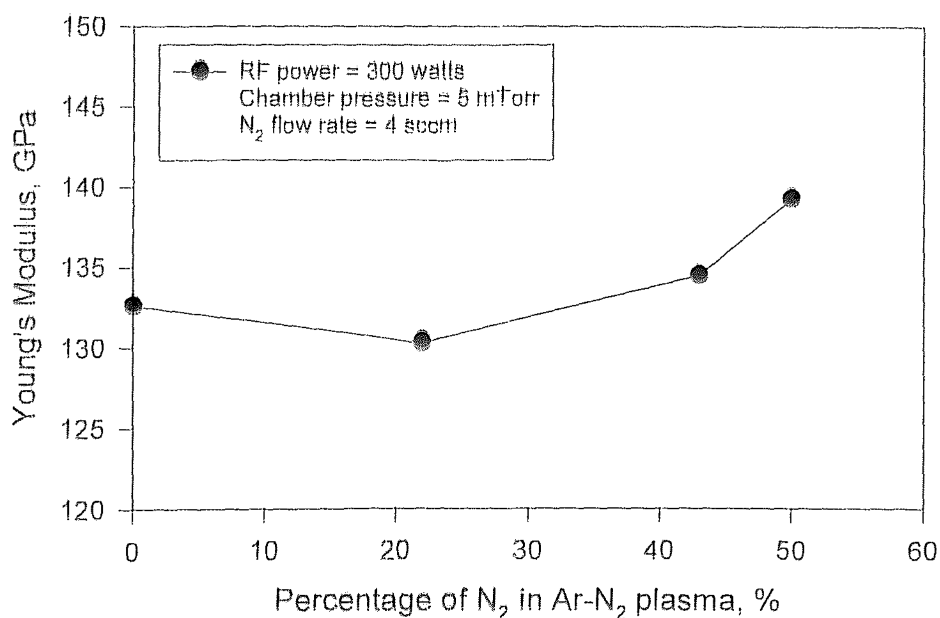

Figure 5.7: Dependence of Young's modulus on nitrogen composition in Ar-N_2 plasma.

Raman spectra of most of the film deposited by reactive magnetron sputtering showed a convolution of Raman active G-band (graphitic at 1590 cm^{-1}) and D band (disordered carbon phase, at 1360 cm^{-1}) similar to that of amorphous diamond like

carbon(a-C). A typical Raman spectra of a carbon nitride thin film deposited by reactive nitrogen in Ar-N_2 mixture is shown in Fig. 5.8.

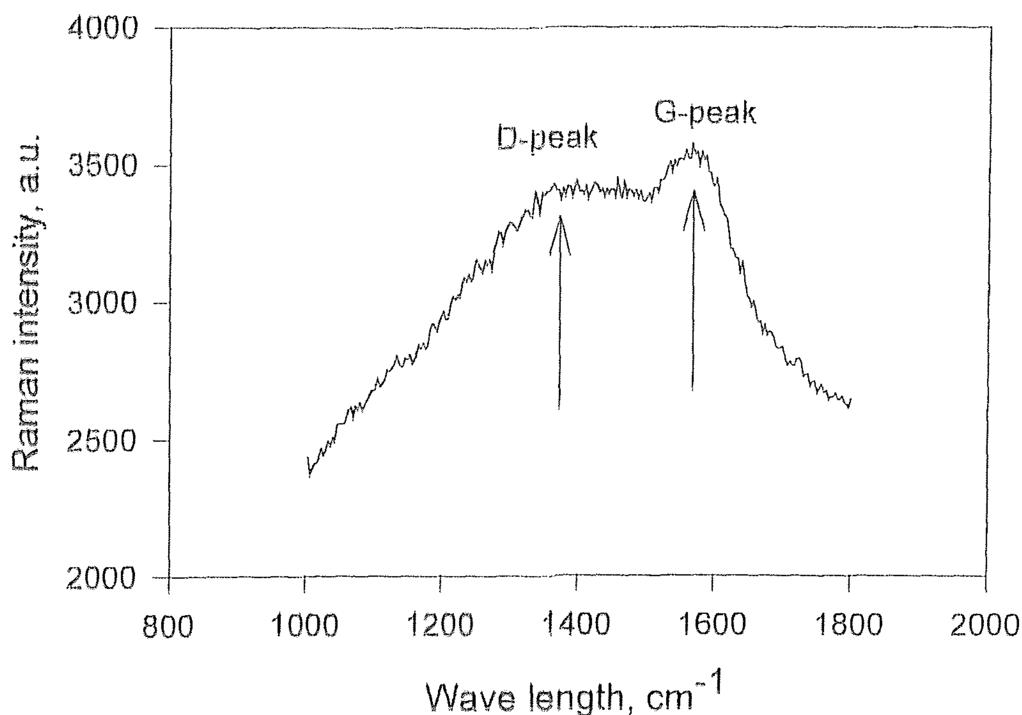

Figure 5.8: Raman spectra of carbon nitride thin film (deposited at 300 Watts RF power, 5 mTorr pressure, 23% nitrogen in Ar-N2 plasma and at 4 sccm of N_2 flow rate).

5.4 Characterization of Cs Enhanced Negative Carbon Ion Source

Current absorbed at the substrate as a measure of flux of charged species toward the substrate was plotted against cesium oven temperature to determine the optimum operating temperature of the oven The experiment was performed in presence of a Ar/Cs plasma at a flow rate of 4 sccm of Ar and at 100 watts RF power. The result is shown in Fig. 5.9. It was observed that absorbed current increased almost linearly from 7 mA to

14 mA for a temperature rise of cesium oven from 25°C to 200°C. Beyond this temperature, absorbed current increased sharply and reached to a maximum value of 43 mA at 225°C. It is interesting to note that above about 225°C, absorbed current started to decrease.

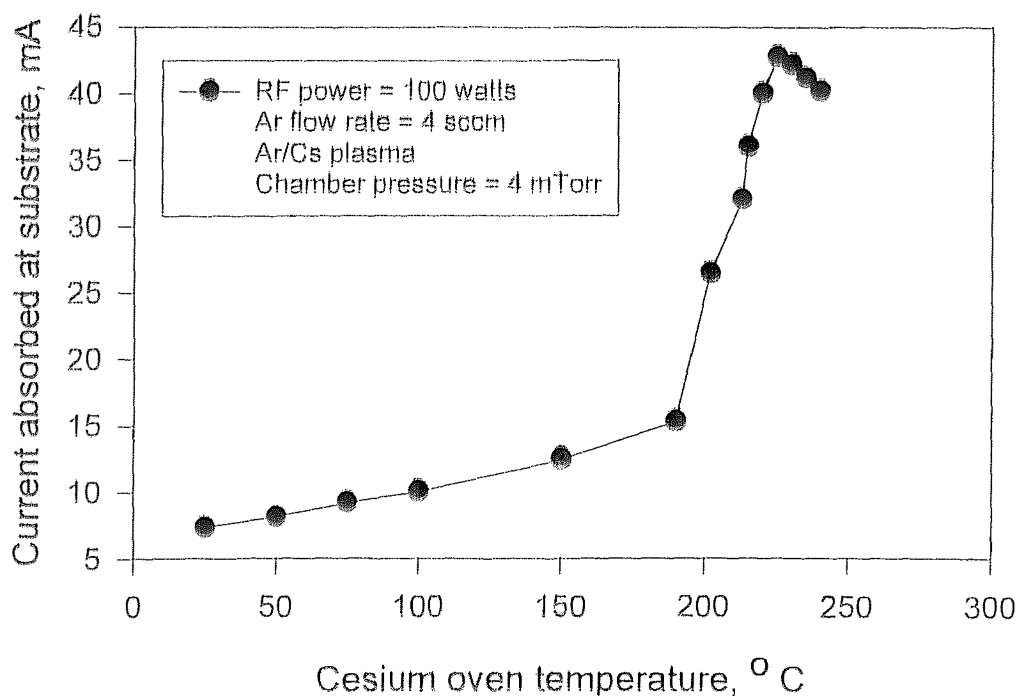

Figure 5.9: Dependency of absorbed current at the substrate on cesium oven temperature.

At low temperature (<200°C) region, absorbed current increased slowly probably due to insufficient Cs vapor in the chamber. For temperature between 200-225 °C, sudden rise of absorbed current was observed due to sufficient cesium vapor to form a fractional monolayer of cesium on the target uniformly to reduce the surface work

function to enhance ejection of negatively charged sputtered carbon. Also excess cesium remain at vapor phase at higher temperature instead of adsorbing on chamber wall and ionized in presence of plasma. It is believed that these were the two reasons for sharp sudden increase of current. For even higher temperature, charged species would undergo increased coulombic interaction due to excessive cesium in vapor phase and as a consequence, flux of ions toward the substrate decreased. There might be another reason that adsorbed cesium on the target started to desorb at higher temperature and ejection of negatively charged carbon ions became less pronounced.

The effect of cesium oven temperature on deposition rate in presence of a Ar-Cs plasma at 100 watts RF power and 3 mTorr chamber pressure is shown in Fig. 5.10

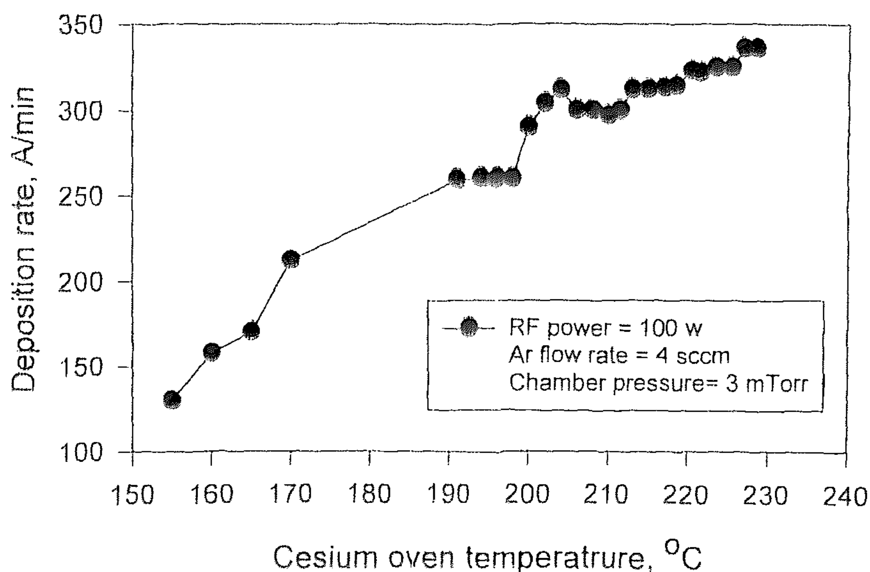

Figure 5.10: Variation of deposition rate with cesium oven temperature.

It is interesting to note that deposition rate in presence of cesium was observed to increase by order of magnitude compared to that in pure Ar plasma at comparable deposition condition (Fig. 5.1). Deposition rate also observed to increase with cesium oven temperature. Deposition rate increased from 125 A/min to about 340 A/min for an increase of cesium oven temperature from 155-230°C.

The effect of chamber pressure on current absorbed at the substrate at 50 Watts RF power and at constant Cs partial pressure of 0.1 mTorr is shown in Fig. 5.11. The temperature of the Cs oven was maintained at 220°C.

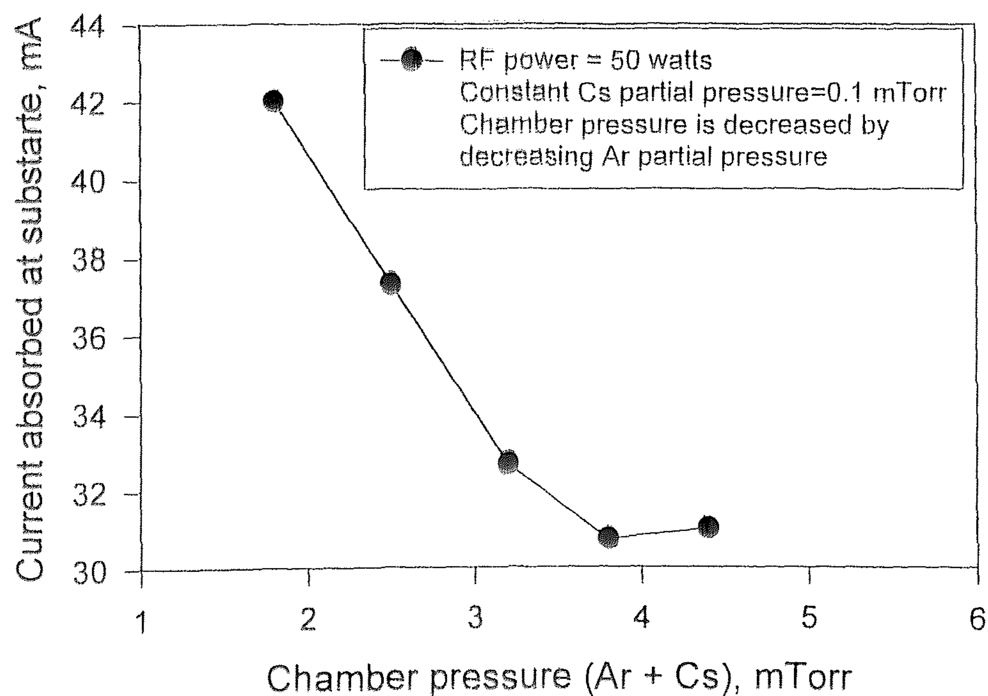

Figure 5.11: Current absorbed at the susbstrate vs. chamber pressure.

The absorbed current decreased from 42 mA to about 31 mA for an increase of pressure from about 1.6 to 3.8 mTorr. However, with further increase of pressure, current was observed to be less sensitive to chamber pressure.

Effect of positive bias voltage applied at ion extraction lens on the top of the sputter gun on current absorbed at the substrate was studied since the the cesium enhanced negative carbon ion source was designed to achieve 150-200 eV negative carbon ions.

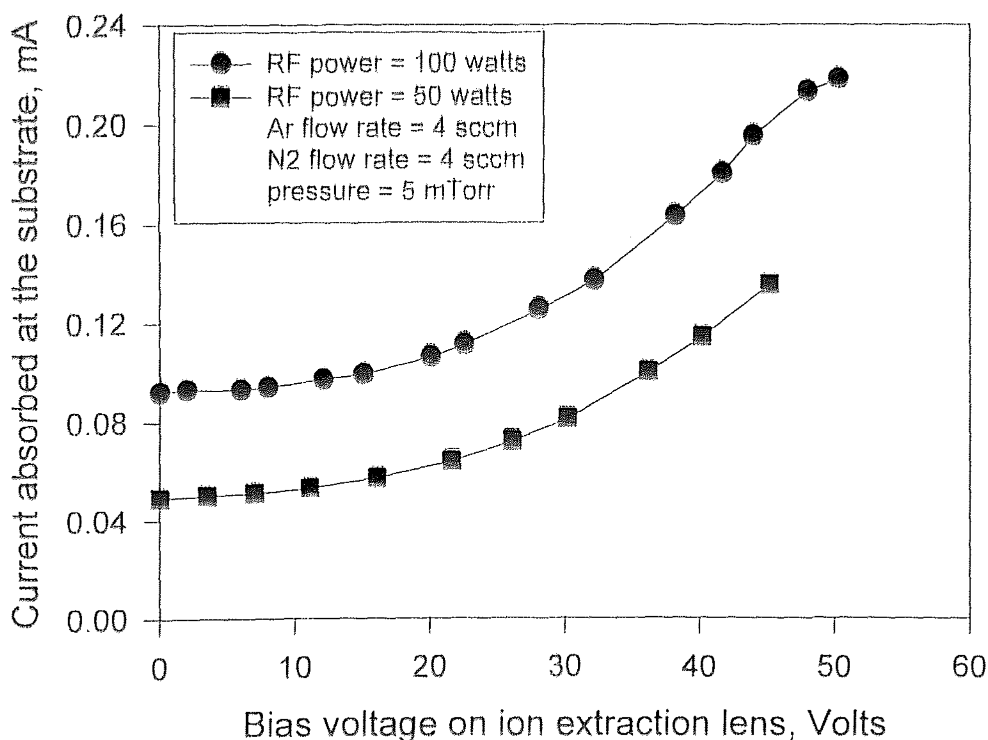

Figure 5.12: Variation of current absorbed at the substrate with positive bias voltage applied at ion extraction lens.

The experiments were performed at 100 and 50 watts of RF power, 5 mTorr chamber pressure and at 4 sccm flow of both Ar and nitrogen. The result is shown in Fig. 5.12. However, it was not possible to apply bias voltage at the ion extraction lens higher than 50 volts due to strong arching in the chamber. Several RF blocking filters were used assuming that arching was due dc/RF interaction but it was not possible to solve the problem. Clear and further understanding of plasma characterisrics is required to minimize strong arching inside the chamber in order to improve the performance of the negative carbon ion source, more specifically the applied extraction bias before arching occurs.

CHAPTER 6

CONCLUSIONS

Microscopically smooth film of carbon nitride were synthesized by reactive magnetron sputtering of graphite target in Ar-N_2 plasma mostly at 300 Watts. The deposition rate and flux of charged species toward the substrate were studied for different process condition. It was observed that nitrogen composition in plasma gas mixture has a strong effect on mechanical properties of the film. The films were amorphous in structure and similar to diamond-like carbon films according to Raman spectra. The microhardness of the film was found to be 10-15 GPa, comparable to that of diamond like carbon films but moderately harder than the silicon substrate. Scratch resistance of the film was found to increase substantially (from 0.07 to 0.9 N) with increasing nitrogen composition in plasma, leading to a possible explanation that the nitrogen leads to formation C-N complexes that act as a lubricant for the hard film.

Further understanding and/or modification of the negative carbon ion source is required to minimize arcing in the chamber and to accelerate negative carbon ions by applying positive voltage on ion extraction lenses.

Based on the results presented, it can be suggested that a two layer film of carbon nitride and diamond-like carbon might be useful to make a hard, lubricating film for commercial bearing and shaft housing applications

REFERENCES

1. Sung, C.M., and M. Sung, "Carbon nitride and other speculative superhard materials", *J. Materials Chemistry and Physics*, vol. 43, pp. 1-18, **1996**.

2. Cohen, M. L., *Phys. Rev. B*, vol 32, pp 7988-7990, **1985**.

3. Knittle, E., *Nature*, vol 337, pp. 349-351, **1989**.

4. Liu, A. Y., and M. L. Cohen, "Prediction of New Low Compressibility Solids", *Science*, vol 41, pp. 841-845, **1989**.

5. Guo, H. Y., and W. Y. Ching, *Phys. Rev. B*, vol 50, pp. 11231-11235, **1994**.

6. Teter, D. M., and R. J. Hamley, *Science*, vol 271, pp. 53-57, **1996**.

7. Han, H. X., and B. J. Feldman, *Solid State Commun.*, vol 65, pp. 921-926, **1988**.

8. Sekine, T., H. Kanda, Y. Bando, and M. Yokoyama, *J. Mater Sci. Lett.*, vol 9, pp. 1375-1377, **1990**.

9. Yang, Y. W., and K. A. Nelson, *J. Mater. Res.*, vol 10, pp. 41-45, **1995**.

10. Wixom, M. R., *J. Am. Ceram. Soc.*, vol 73, pp. 1973-1979, **1990**.

11. Maya, L., D. R. Cole, and E. W. Hagman, *J. of Am Ceram. Soc.*, vol 74 (7), pp. 1686-1690, **1991**.

12. Murzin, I. H., G. S. Tompa, E. W. Forsythe, and J. Wei, *J. Vac. Sci. & Tech.*, vol. A15 (3), pp. 1179-1184, **1997**.

13. Murzin, I. H., G. S. Tompa, J. Wei, V, Muratov, and T. Fisher, *Mat. Res. Soc. Proc*, vol. 438, pp. 569-574, **1997**.

14. Niu, C. M., Y. Z. Liu, and C. M. Lieer, *Science*, vol. 261, pp. 334-339, **1993**.

15. Ren, Z. M., Y. C. Du, Y. X. Qiu, J. D. Wu, Z. F. Ying, X. X. Xiong, and F. M. Li, *Phys. Rev. B*, vol. 51, pp. 5274-5277, **1995**.

16. Chen, Y., L. P. Guo, and E. G. Wang, *J. Phys. Condense Matt.*, vol. 8, pp. 685-690, **1996**.

17. Chen, Y., L. P. Guo, and E. G. Wang, *Philo. Mag. Lett.*, vol. 75 (3), pp. 155-158, **1997**.

18. Chen, Y., L. P. Guo, and E. G. *Wang, J. Crystal Growth*, vol. 179, pp. 515-520, **1997**.

19. Chen, Y., L. P. Guo, and E. G. Wang, *Mater. Sci. lett.,* vol. 16, pp. 594-597, **1997**.

20. Ohring, M, *The Material Science of Thin Films*, Academic Press, Inc., California, Ch. 3, pp. 79-144, **1992**.

21. Westwood, W. D., *Physics of Thin Films*, vol. 14, Edited by M. H. Francombe and J. L. Vossen, Academic Press, New York, **1989**.

22. Chen, M. Y., X. Lin, V. P. Dravid, Y. W. Chung, M. S. Wong, and W.D. Sproul, *Surface and Coating Technology*, vol. 54, pp. 360-364, **1992**.

23. Chen, M. Y., X. Lin, V.P. Dravid, Y. W. Chung, M. S. Wong, and W.D. Sproul, *STLE Tribology Transactions*, vol. 36 (3), pp. 491-495, **1993**.

24. Li, D., Y. W. Chung, S. Yang, M. S. Wong, F. Abidi, and W. D. Sproul, *J. Appl. Phys.*, vol. 74 (1), pp. 219-224, **1993**.

25. Torng, C. J., J. M. Sivertsen, J. H. Judy, and C. Chang, *J. Mater. Res.*, vol. 5 (11), pp. 2490-2494, **1990**.

26. Bousetta, A., M. Lu, A. Bensaoula, and A. Schultz, *Appl. Phys. Lett.*, vol. 65 (6), pp. 696-699, **1994**.

27. Ogata, K., J. F. D. Chubaci, and F. Fujimoto, *J. Appl. Phys.*, vol. 76 (6), pp. 3791-3794, **1994**.

28. Rossi, F., B. Andre, A. van Veen, P. E. Mijnarends, H. Schut, F. Labohm, H. Dunlop, M. P. Deplancke, and K. Hubbard, *J. Mater. Res.*, vol. 9 (9), pp. 2441-2446, **1994**.

29. Lin, S., K. Noonan, B. J. Feldman, D. Min, and M. T. Jones, *Sol. State Comm.*, vol. 80 (2), pp. 101-105, **1991**.

30. Viehland, J., S. Lin, B. J. Feldman, K. Kilgore, and M. T. Jones, *Sol. State Comm.*, vol. 80 (8), pp. 597-600, **1991**.

31. Ricci, M., M. Trinquecoste, F. Auguste, R. Canet, P. Delhaes, C. Guimon, G. Pfister-Guilouzo, B. Nysten, and J.P. Issi, *J. Mater. Res.*, vol. 8 (3), pp. 480-485, **1993**.

32. Matsumoto, O., T. Kotaki, H. Shikano, K. Takemure, and S. Tanaka, *J. Electrochem. Soc.*, vol. 141 (2), L16, **1994**.

33. Tompa, G. S., I. H. Murzin, S. I. Kim, Y. O. Ahn, B. Gallois, T. E. Fischer, and E. W. Forsythe, *Mat. Res. Soc. Symp. Proc.*, vol. 396, pp. 545-50, **1996**.

34. Boyd, K. J., and J. W. Rabalais, *Int. J. Modern Phys. B*, vol. 9 (27), pp. 3527-3558, **1995**.

35. Merchant, A. R., D. G. McCulloch, Y. Yin, L. Hall, and E. G. Gerstner, *J. Appl. Phys.*, vol. 79 (1), pp. 6914-6919, **1996**.

36. Li, D., S. Lopez, and Y. W. Chung, *J. Vac. Sci. & Technol.*, vol. A13 (3), pp. 1063-1066, **1995**.

37. Li, D., Y. W. Chung, and S. Yang, *J. Vac. Sci. & Technol.*, vol A12 (4), 1995, pp. 1470-1473, **1995**.

38. Kumar, S., K. S. A. Butcher, and T. L. Tansley, *J. Vac. Sci. & Technol.*, vol. A14 (5), pp. 2687-2692, **1996**.

39. Hammer, P., M. A. Baker, C. Lenardi, and W. Gissler, *Proc. Int. Conf. On Metallurgical Thin Films*, San Diego, 1996.

40. Riviere, D. Texier, J. Delafond, M. Jaouen, E. L. Mathe, and J. Chaumont, *Materials Letters*, vol. 22, pp. 115-118, **1995**.

41. Boyd, K. J., D. Marton, S. S. Todorov, A. H. Al-Bayati, R. A. Zuhr, and J. W. Rabalais, *J. Vac. Sci. & Technol.*, vol. A13 (4), p. 2110, **1995**.

42. Marton, D., A. H. Al-Bayati, S. S. Todorov, K. J. Boyd, and J. W. Rabalais, *Nucl. Instr. Meth. in Phys. Res.*, vol. B90, pp. 277-281, **1994**.

43. Marton, D., K. J. Boyd, A. H. Al-Bayati, S. S. Todorov, and J. W. Rabalais, *Phys. Rev. Lett.*, vol. 73 (1), pp. 118-123, **1994**.

44. Fernandez, A., P. Prieto, C. Quiros, J. M. Sanz, J. M. Martin, and B. Vacher, *Appl. Phys. Lett.*, vol. 69 (6), pp. 764-766., **1996**.

45. Wu, Z., Y. Yu, and X. Liu, *Appl. Phys. Lett.*, vol. 68 (9), pp. 1291-1294, **1996**.

46. Zhang, Y. Z. Zhou, and H. Li, *Appl. Phys. Lett.*, vol. 68 (9), pp. 634-637, **1996**.

47. Krieder, K. G., M. J. Tarlov, G. J. Gillen, G. E. Poirier, L. H. Robins, L. K. Ives, W. D. Bowers, R. B. Marinenko, and D. T. Smith, *J. Mater. Res.*, vol. 10 (12), **1995**.

48. Tompa, G. S., J. L. Lopes, and G. Wohlrab, *Rev. Sci. Instr.*, vol. 58(8), p. 1536, **1987**.

49. Tompa, G. S., W. E. Carr, and M. Seidl, *Appl. Phys. Lett.*, vol. 48 (16), p. 1048, **1996**.

50. Kittel, C., *Introduction to Solid State Physics*, John Wiley Publications, New York, p. 131, **1986**.